Secondary aerosol formation alters CCN activity in the North China Plain

Jiangchuan Tao[1, 2], Ye Kuang[1, 2], Nan Ma[1, 2], Juan Hong[1, 2], Yele Sun[3, 4, 5], Wanyun Xu[6], Yanyan Zhang[1], Yao He[3], Qingwei Luo[1], Linhong Xie[1, 2], Hang Su[7], Yafang Cheng[7]

[1]Institute for Environmental and Climate Research, Jinan University, Guangzhou, Guangdong 511443, China

[2]Guangdong-Hongkong-Macau Joint Laboratory of Collaborative Innovation for Environmental Quality, Guangzhou, China

[3]State Key Laboratory of Atmospheric Boundary Layer Physics and Atmospheric Chemistry, Institute of Atmospheric Physics, Chinese Academy of Sciences, Beijing 100029, China

[4]College of Earth and Planetary Sciences, University of Chinese Academy of Sciences, Beijing 100049, China

[5]Center for Excellence in Regional Atmospheric Environment, Institute of Urban Environment, Chinese Academy of Sciences, Xiamen 361021, China

[6]State Key Laboratory of Severe Weather, Key Laboratory for Atmospheric Chemistry, Institute of Atmospheric Composition, Chinese Academy of Meteorological Sciences, Beijing, 100081, china

[7]Multiphase Chemistry Department, Max Planck Institute for Chemistry, Mainz 55128, Germany

Correspondence to: Jiangchuan Tao (taojch@jnu.edu.cn) and Nan Ma (nan.ma@jnu.edu.cn)

Abstract:

Secondary aerosols (SA, including secondary organic and inorganic aerosols, SOA and SIA) are predominant components of aerosol particles in the North China Plain (NCP) and its formation has significant impacts on the evolution of particle size distribution (PNSD) and hygroscopicity. Previous studies have shown that distinct SA formation mechanisms can dominate under different relative humidity (RH). This would lead to different influences of SA formation on the aerosol hygroscopicity and PNSD under different RH conditions. Based on the measurements of size-resolved particle activation ratio (SPAR), hygroscopicity distribution (GF-PDF), $PM_{2.5}$ chemical composition, PNSD, meteorology and gaseous pollutants in a recent field campaign, McFAN (Multiphase chemistry experiment in Fogs and Aerosols in the North China Plain), conducted during the autumn-winter transition period in 2018 at a polluted rural site in the NCP, the influences of SA formation on cloud condensation nuclei (CCN) activity and CCN number concentration (N_{CCN}) calculation under different RH conditions were studied. Results suggest that during daytime, SA formation could lead to a significant increase in N_{CCN} and a strong diurnal variation in SPAR at Super-saturations lower than 0.07%. During periods with daytime minimum RH exceeding 50% (high RH conditions), SA formation significantly contributed to the particle mass/size changes in a broad size range of 150 nm to 1000 nm, led to N_{CCN} increases within the size range of 200 nm to 300 nm, and mass concentration growth mainly for particles larger than 300 nm. During periods with daytime minimum RH below 30% (low RH conditions), SA formation mainly contributed to the particle mass/size and N_{CCN} changes for particles smaller than 300 nm. As a result, under the same amount of mass increase induced by SA formation, the increase of N_{CCN} was stronger under low RH conditions and weaker under high RH conditions. Moreover, the diurnal variations of SPAR parameter (inferred from CCN measurements) due to SA formation varied with RH conditions, which was one of the largest uncertainties within N_{CCN} predictions. After considering the SPAR parameter (estimated through the number fraction of hygroscopic particles or mass fraction of SA), the relative deviation of N_{CCN} predictions were reduced to within 30%. This study highlights the impact of SA formation on CCN activity and N_{CCN} calculation, which provides guidance for future improvements of CCN predictions in chemical-transport models and climate models.

1. Introduction

Cloud condensation nuclei (CCN) activity of aerosol particles describes its ability to activate and grow into cloud droplets at given supersaturations and thus has important impacts on cloud microphysics and the aerosol indirect effect on climate. CCN activity is dependent on the physicochemical properties of aerosol particles, including particle size distributions, hygroscopicity (determined by chemical composition) and mixing state. Thus, atmospheric processes influencing these aerosol properties may exert influences on CCN activity.

Secondary aerosols (SA) formation contributes greatly to aerosol populations and impacts CCN properties in many ways, generally increasing CCN number concentrations (N_{CCN}) and leading to changes in the CCN activity (Wiedensohler et al., 2009; Kerminen et al., 2012; Wu et al., 2015; Farmer et al., 2015; Ma et al., 2016; Zhang et al., 2019 and reference therein). Differences in precursor and oxidant concentrations as well as SA formation mechanisms lead to particle size growth in different size ranges (Dal Maso et al., 2005; Kulmala et al., 2007; Zhang et al., 2012; Farmer et al., 2015; Cheng et al., 2016; Kuang et al., 2020c), thus would impact CCN activities in different ways. SA formation includes both the formation and subsequent growth of new particles (New Particle Formation, NPF), and the growth of existing particles. NPF can directly provide particles large enough to act as CCNs (Wiedensohler et al., 2009; Kerminen et al., 2012; Farmer et al., 2015), generally affecting aerosol particles smaller than 100 nm, thereby elevating N_{CCN} at higher supersaturations (SSs>0.2%) (Wiedensohler et al., 2009; Kerminen et al., 2012; Ma et al., 2016; Zhang et al., 2019 and reference therein). SA formation on existing particles, especially under polluted conditions, significantly adds mass to and changes the chemical composition of accumulation mode particles (Farmer et al., 2015), thus affecting CCN at lower SSs (<0.2%) (Wiedensohler et al., 2009; Mei et al., 2013; Yue et al., 2016; Thalman et al., 2017; Duan et al., 2018). SSs varies greatly among different clouds categories. Cumulus clouds are formed under higher SSs and are thus mostly influenced by Aitken mode particles formed in NPF events (Reuter et al., 2009; Gryspeerdt and Stier, 2012; Fan et al., 2016; Jia et al., 2019 and reference therein). Stratus clouds and fogs that exert stronger effects on climate and environment, however, are generally formed at SSs lower than 0.2%, indicating that only accumulation mode particles can serve as CCN (Ditas et al., 2012; Hammer et al., 2014a, b; Krüger et al., 2014; Shen et al., 2018). Numerous studies have investigated the impact of NPF on CCN (Gorden et al., 2016; Ma et al., 2016; Yu et al., 2020 and reference therein), however, only few studies have focused on the influence of SA formation on CCN activity of accumulation mode particles, which might exhibit strong climate and environment impacts and urgently requires attention.

80   SA formation affects CCN activity of accumulation mode particles not only by enlarging their

81   size, but also by changing their chemical compositions. At a specific particle size, the CCN activity is

82   determined both by the chemical composition of particles, which originally were and stayed this size,

83   and that of particles, which grew into this size via added SA mass. These two groups of particles can

84   exert different variations to CCN activity at the same particle size (Wiedensohler et al., 2009 and

85   reference therein). In general, the SA formation can increases the hygroscopicity of particles by adding

86   chemical compounds with lower volatility and higher oxidation state, which are usually more

87   hydrophilic, thereby enhancing CCN activity of accumulation mode particles (Mei et al., 2013; Yue et

88   al., 2016). However, CCN activity may also remain unchanged (Wiedensohler et al., 2009) or be

89   weakened in some cases (Thalman et al., 2017; Duan et al., 2018). In SA formation observed in central

90   Amazon forests, Thalman et al. (2017) reported enhanced CCN activity in dry season while constant

91   CCN activity in wet season. In SA formation events under polluted conditions in Guangzhou (Pearl

92   River Delta, China), Duan et al. (2018) found that bulk CCN activity can be enhanced in summer due

93   to the formation of large and inorganic-rich particles, but weakened in winter due to the formation of

94   small and organic-rich particles, where RH seemed to have been an important factor in the variations

95   of bulk CCN activity due to different particle formation pathways. Aside from variations of particle

96   chemical composition, changes in aerosol mixing states caused by SA formation can also change CCN

97   activity (Su et al., 2010; Rose et al., 2011; Cheng et al., 2012). The fast condensation of SA components

98   on accumulation mode particles led to the turnover of soot particle mixing state from externally to

99   internally mixed, which contributed mostly to enhancements of CCN activity (Cheng et al., 2012).

100   Thus, SA formation influences the CCN activity of accumulation mode particles through its integrated

101   impacts on their size, hygroscopicity and mixing state, which requires more detailed and

102   comprehensive investigations.

103   The North China Plain (NCP) frequently experiences severe aerosol pollution due to both

104   strong emissions of primary aerosol and strong SA formation caused by the abundance of gaseous

105   precursors and oxidants (Zheng et al. ACP, 2015; Liu et al., 2010; Huang et al., 2014; Xu et al., 2019).

106   In the SA formation events on the NCP, both aqueous-phase processes and gas-phase photochemical

107   processes can play important roles, depending on atmospheric conditions such as RH (Hu et al., 2016;

108   Xu et al., 2017a; Wang et al., 2019). A recent observational study on the NCP found that SA formation

109   dominantly contributed to different particle size since SA formation mechanisms varied with RH

110   conditions (Kuang et al., 2020c). Under dry conditions, SA were mainly formed through gas-phase

111   photochemical processing and mostly added mass to accumulation mode particles. While under high

112   RH conditions or super-saturated conditions, SA was also formed in aqueous phase, contributing to

113 the formation of both accumulation mode and coarse mode particles. The difference in particle size

114 where SA formation took place and the difference in SA chemical compositions could result in distinct

115 variations of CCN activity, which has not been evaluated yet. In this study, we will study the influence

116 of SA formation on Size-resolved Particle Activation Ratio (SPAR) of accumulation mode particles

117 in the NCP under different RH conditions, which fills a gap of knowledge within CCN studies in the

118 NCP and may provide guidance for the improvement of current CCN parameterization schemes in

119 chemical-transport and climate models.

120 **2. Method:**

121 2.1. Measurements

122 2.1.1. Site

123   Under the framework of McFAN (Multiphase chemistry experiment in Fogs and Aerosols in

124 the North China Plain) (Li et al., 2021), from 16th November to 16th December 2018, physical and

125 chemical properties of ambient aerosol particles as well as meteorological parameters were

126 continuously measured at the Gucheng site in Dingxing county, Hebei province, China. This site is an

127 Ecological and Agricultural Meteorology Station (39°09'N, 115°44'E) of the Chinese Academy of

128 Meteorological Sciences, which is located between Beijing (~100km) and Baoding (~40km), two

129 mega cities in the North China Plain, and surrounded by farmlands and small towns. Measurements at

130 this site can well represent the polluted background conditions of the NCP. All aerosol measurement

131 instruments were placed in a container with temperature maintained at 24 °C, while conventional trace

132 gas instruments including CO were housed in an air-conditioned room on a two-story building located

133 ~80 meters to the south of the container, with no taller buildings between them blocking the air flow.

134 2.1.2 Instrumentation

135   In this study, ambient aerosol was sampled by an inlet system consisting of a PM10 inlet

136 (Rupprecht & Patashnick Co., Inc., Thermo, 16.67 L/min), a Nafion dryer that dried relative humidity

137 to below 30% and an isokinetic flow splitter directing the air sample to each instrument.

138   A DMA-CCNC system measured SPAR at five supersaturations (SSs), 0.05%, 0.07%, 0.2%,

139 0.44% and 0.81%, with a running time of 20 min for 0.05% and 10 min for the other SSs. This system

140 consisted of a differential mobility analyzer (DMA model 3081; TSI, Inc, MN USA), a condensation

141 particle counter (CPC model 3772; TSI, Inc., MN USA) and a continuous-flow CCN counter (model

142 CCN200, Droplet Measurement Technologies, USA; Roberts and Nenes, 2005). The system was

143 operated in a size-scanning mode over the particle size range from 9 to 400 nm. SPAR can be obtained

144 by combining the measurements of CPC and CCNC at different particle size. The sample and sheath

flow rate of the DMA were set to 1 lpm and 5 lpm, respectively, hence the resultant measured particle diameter ranged from 9 nm to 500 nm. Since the low number concentration of particles above 300 nm could lead to large uncertainty in CCNC counting, the measurements for particles larger than 300 nm were excluded, except for 0.05% SS. In order to characterize the variations of particles with low hygroscopicity of about 0.1, SPAR measurement up to about 400nm is used at 0.05% SS. There are 12 size distribution scans during a complete 1-hour cycle, with four scans for first SS and two scans for each of the rest four SSs. Only the last scan for each SS is used as the CCNC needs time for SS stabilization. The SSs of CCNC were calibrated with monodispersed ammonium sulphate particles (Rose et al., 2008) both before and after the campaign. The flowrates were checked regularly (every few days) during the campaign, as the flows (sample flow and sheath flow) of the instrument can affect both the counting of droplets and the SS in the column. A modified algorithm based on Hagen and Alofs (1983) and Deng et al. (2011, 2013) was used to correct the influence of multiple-charge particles and DMA transfer function on SPAR. Details about the system are described in Ma et al. (2016) and the description about the inversion method can be found in the supplements.

Non-refractory particulate matter (NR-PM) including SO_4^{2-}, NO_3^-, NH_4^+, Cl^- and organics with dry aerodynamic diameters below 2.5 μm was measured by an Aerodyne Time-of-Flight Aerosol Chemical Speciation Monitor (ToF-ACSM hereafter) equipped with a $PM_{2.5}$ aerodynamic lens (Williams et al., 2010) and a capture vaporizer (Xu et al., 2017b; Hu et al., 2017a) at 2-minute time resolution. The ToF-ACSM data were analyzed with the standard data analysis software (Tofware v2.5.13; https://sites.google.com/site/ariacsm/, last access: 21 January 2020). The organic mass spectra from *m/z* 12 to 214 were analyzed with an Igor Pro based positive matrix factorization (PMF) evaluation tool (v3.04) and then evaluated following the procedures described in Zhang et al. (2011). The chosen five-factor solution includes four primary factors i.e. hydrocarbon-like OA (HOA), cooking OA (COA), biomass burning OA (BBOA), and coal combustion OA (CCOA), and a secondary factor, i.e. oxygenated OA (OOA). More detailed descriptions on the ACSM measurements and data analysis can be found in Kuang et al. (2020b) and Sun et al. (2020).

A Humidified Tandem differential mobility analyzer (HTDMA, Tan et al., 2013) measured the size-resolved aerosol growth factor (GF) at 90% RH. The sampled particles were subsequently charged by a neutralizer (Kr85, TSI Inc.) and size selected by a DMA (DMA1, model 3081L, TSI Inc.). A Nafion humidifier (model PD-70T-24ss, Perma Pure Inc., USA) was used to humidify the monodisperse particles with a specific diameter (D_d) at a fixed RH of (90 ± 0.44) % and then the number size distribution of the humidified particles (D_{wet}) was measured by another DMA (DMA2,

model 3081L, TSI Inc.) and a condensation particle counter (CPC, model 3772, TSI Inc.). Thus, GF of the particles can be calculated as:

$$GF = \frac{D_{wet}}{D_d} \tag{1}$$

During the campaign, four dry mobility diameters (60, 100, 150, and 200 nm) were selected for the HTDMA measurements. A full scan takes about 1 hour in order to cover the four sizes. Regular calibration by using standard polystyrene latex spheres and ammonium sulfate were performed to ensure the instrument functioned normally. The tandem differential mobility analyzer (TDMA) inversion algorithm (Gysel et al., 2009) was applied to calculate the Probability Density Function of GF (GF-PDF). More details about this system can be found in Cai et al. (2018) and Hong et al. (2018).

Particle number size distributions (PNSDs) were measured by combining the measurements of a scanning mobility particle sizer (SMPS, TSI model 3080) and an aerodynamic particle sizer (APS, TSI Inc., Model 3321), that measured particle mobility diameter size distributions in the range of 12 nm to 760 nm and particle aerodynamic diameter size distribution in the range of 700 nm to 10 μm, respectively. A commercial instrument from Thermo Electronics (Model 48C) was used to measure CO concentration. Besides monthly multipoint calibrations and weekly zero-span check, additional 6-hourly zero checks were also performed for the CO instrument.

2.2. Data processing

2.2.1. Aerosol hygroscopicity and cloud activation: κ-Köhler theory

The ability of particles to act as CCN and its dependence on particle size and particle chemical composition on CCN activity can be described by the Köhler theory (Köhler, 1936). A hygroscopic parameter κ is calculated based on the κ-Köhler theory (Petters and Kreidenweis. 2007) to evaluate the influence of particle chemical compositions:

$$\kappa = \left(\frac{D_{wet}^3 - D_d^3}{D_d^3} \right) \left[\frac{1}{S} \exp \left(\frac{4\sigma_{s/a} M_w}{R T \rho_w D_{wet}} \right) - 1 \right], \tag{1}$$

where S represents the saturation ratio, ρ_w is the density of water, M_w is the molecular weight of water, $\sigma_{s/a}$ is the surface tension of the solution/air interface, R is the universal gas constant, T is the temperature, D_d is the diameter of dry particle and D_{wet} is the diameter of the humidified particle. In this study, $\sigma_{s/a}$ is assumed to be the surface tension of pure water/air interface. Based on the κ-Köhler theory, the surface equilibrium water vapor saturation ratio of particles with a specific κ at different wet particle size can be calculated, and the maximum value of surface equilibrium saturation ratio (which is generally supersaturated) is defined as the critical SS for CCN activation. As a result, the

variation of the critical diameter for particles with different hygroscopicity (or GF at a specific RH) at different SSs can be determined.

2.2.2. Aerosol growth factor and its probability density function

In practice, the growth factor probability density function (GF-PDF) was inversed from the measured GF distribution using a TDMAinv algorithm (Gysel et al., 2009). After obtaining the GF-PDF, the ensemble average GF and corresponding critical diameter under a certain SS ($D_{a,GF}$) can be calculated. Furthermore, the number fraction and the weighted-average GF of hygroscopic particles ($\kappa > 0.1$ and GF(90%, 200 nm)>1.22) were calculated as:

$$NF_{hygro} = \int_{1.2}^{\infty} PDF(GF) \times dGF \qquad (2)$$

$$GF_{hygro} = \int_{1.2}^{\infty} GF \times PDF(GF) \times dGF \qquad (3)$$

Based on the κ-Köhler theory, the hygroscopicity parameter κ and corresponding critical diameter ($D_{a,hygro}$) under a certain SS for particles with GF_{hygro} can be calculated. As GF_{hygro} is higher than the average GF, $D_{a,hygro}$ is smaller than $D_{a,GF}$.

2.2.3 Calculations of aerosol hygroscopicity from aerosol chemical-composition measurements

For the calculation of aerosol hygroscopicity parameter κ based on measured chemical composition data (κ_{chem}), detailed information on the chemical species are needed. The ACSM can only provide bulk mass concentrations of SO_4^{2-}, NO_3^-, NH_4^+, Cl^- ions and organic components, which cannot be used to calculate size resolved hygroscopicity. However, in the North China Plain, accumulation mode particles are the dominant contributors to the bulk particle mass concentration (Liu et al., 2014; Xu et al., 2015; Hu et al., 2017b) and thus the bulk chemical compositions can be used as a proxy for that of accumulation mode particles. For the inorganic ions, a simplified ion pairing scheme was used to convert ion mass concentrations to mass concentrations of corresponding inorganic salts (Gysel et al., 2007; Wu et al., 2016). Thus, mass concentrations of SO_4^{2-}, NO_3^-, NH_4^+ and Cl^- are specified into ammonium sulfate (AS), ammonium nitrate (AN), ammonium chloride (AC) and ammonium bisulfate (ABS), for which the κ values under super-saturated conditions were specified according to Petters and Kreidenweis (2007). For a given internal mixture of different aerosol chemical species, the Zdanovskii–Stokes–Robinson (ZSR) mixing rule can be applied to predict the overall κ_{chem} using volume fractions of each chemical species (ε_i) (Petters and Kreidenweis, 2007):

$$\kappa_{chem} = \sum_i \kappa_i \cdot \varepsilon_i \qquad (4)$$

236 where κ_i and ε_i represent the hygroscopicity parameter κ and volume fraction of chemical component

237 i in the mixture. Based on Eq.2, κ_{chem} can be calculated as follows:

$$\kappa_{chem}=\kappa_{AS}\varepsilon_{AS}+ \kappa_{AN}\varepsilon_{AN}+\kappa_{ABS}\varepsilon_{ABS}+\kappa_{AC}\varepsilon_{AC}+\kappa_{BC}\varepsilon_{BC}+\kappa_{Org}\varepsilon_{Org} \qquad (5)$$

239 where κ_{BC} is assumed to be zero as black carbon is hydrophilic. κ_{org} and ε_{org} represent κ and volume

240 fraction of total organics. The values of hygroscopicity parameter for inorganic compounds can be

241 found in Table 1 of Kuang et al. (2020b). Large variations in κ_{org} has been reported in former studies

242 and a linear relationship between κ_{org} and organic aerosol oxidation state (f44) was detected in our

243 campaign (Kuang et al., 2020b), which was adopted to calculate κ_{org} in this study:

$$\kappa_{Org}=1.04\times f44-0.02 \qquad (6)$$

245 It should be noted that the κ-Köhler theory is not perfect, even for inorganic compounds.

246 Numerous studies have been focusing on the performance of its application on measurements under

247 different RH conditions (Liu et al., 2011; Wang et al., 2017). And κ_{org} used in this study was

248 determined by the measurement of humidified nephelometer at RH of 85% in Petters and Kreidenweis,

249 (2007), due to the lack of κ_{org} measured under super-saturated conditions. In this study, we focus on

250 the variations of κ values derived from HTDMA and CCN measurement during the SA formation

251 events, rather than the closure between κ values derived using different techniques, which will be

252 addressed in an upcoming study.

253 2.2.4. Fitting parameterization scheme of SPAR

254 In general, the variation in CCN activity of a particle population can be attributed to the

255 variation in the number fraction of hygroscopic particles or its hygroscopicity, which can be indicated

256 by fitting parameters of SPAR curves parameterization. SPAR curves are often parameterized using a

257 sigmoidal function with three parameters. This parameterization assumes aerosols to be an external

258 mixture of apparently hygroscopic particles that can act as CCN and non-hygroscopic particles that

259 cannot be measured by CCNC within the measured particle size range below 400 nm (Rose et al.,

260 2010). SPAR ($Ra(D_p)$) at a specific SS can be described as follows (Rose et al., 2008):

$$Ra(D_p)=\frac{MAF}{2}\left(1+erf\left(\frac{D_p-D_a}{\sqrt{2\pi}\sigma}\right)\right) \qquad (7)$$

262 where erf is the error function. MAF is the asymptote of the measured SPAR curve at large particle

263 sizes. D_a is the midpoint activation diameter and is associated with the hygroscopicity of CCNs. σ is

264 the standard deviation of the cumulative Gaussian distribution function and indicates the heterogeneity

265 of CCN hygroscopicity. As reported by Jiang et al. (2021), based on the investigation of the

covariations between SPAR curves and parameterized hygroscopicity distribution, it was found that the MAF can be used to estimate the number fraction of hygroscopic (thus CCN-active) particles, for aerosol hygroscopicity distributions generally observed in ambient atmosphere, and thus half MAF can be used to represent the number fraction of CCNs to total particles at particle size around D_a. Although the influence of particles whose κ is less than 0.1 on SPAR cannot be considered in this parameterization scheme, significant deviation were only found under higher SSs (Tao et al., 2020) and need not to be considered under the low SSs discussed in this study.

To be noted, the meaning of MAF can be different regard to the SS, and SPAR measurement up to about 400nm is needed for the MAF fitting for SPAR at SS of 0.05% to represent the particles with κ value higher than 0.1. For SPAR at SS of 0.8%, MAF should be 1 at 400 nm diameter. However, a MAF of 1 in this case can lead to overestimations of hygroscopic particle number fraction due to the significant difference between SPAR curves and sigmodal fitting curves. In the former study on SPAR fitting curves in the NCP, it was found that a fitting parameterization with the combination of two sigmodal fitting curves was needed for SPAR fitting at SSs higher than 0.4% (Tao et al., 2020). However, in this study, we investigate SA formation on accumulation mode particles and particle CCN activity at SSs below 0.1%, under which condition non-hygroscopic particles smaller than 400 nm are typically CCN-inactive. The MAF fitted in the particle size range below 400 nm was used to indicate the variations of SPAR that was of the main focus here in this work. In addition, due to the very low N_{CCN} in particle size ranges larger than 400 nm, the deviations of N_{CCN} due to the limited range of measured particle size are also very small.

3. Results

3.1. Overview of the measurements

The timeseries of meteorological parameters, SPAR, N_{CCN} at SS of 0.05% and mass concentration of Non-refractory particulate matter of $PM_{2.5}$ (NR-$PM_{2.5}$), $PM_{2.5}$ SA and $PM_{2.5}$ PA (primary aerosol, defined as the sum of POA) are shown in Fig. 1. During the campaign, $PM_{2.5}$ PA were generally lower than 100 μg m^{-3} under both high and low RH periods. Meanwhile, $PM_{2.5}$ SA can approach about 400 μg m^{-3}, especially during the strong SA formation events under high RH conditions, but can be lower than 100 μg m^{-3} under low RH conditions. Strong diurnal variations were found in SPAR with varying meteorological parameters. During the whole period, the wind speed was generally lower than 4 m s^{-1}, which is in favor of aerosol particle accumulation and SA formation on existing particles. However, RH, N_{CCN}, $PM_{2.5}$ SA and NR-$PM_{2.5}$ mass concentrations revealed very distinct levels before and after 4th Dec, and thus the whole campaign was divided into two stages with different RH and SA pollution conditions: higher RH and stronger SA pollution before 4th Dec, and lower RH and lighter SA pollution after 4th Dec. In the following discussions, the high RH stage corresponds to days before 4th Dec with daily maximum and minimum RH higher than 75% and 50%, respectively. Two events that occurred during 25th Nov to 27th Nov (Event 1) and 30th Nov to 2nd Dec (Event 2), respectively, displayed especially high RH conditions with successive nighttime fogs (blue shaded areas). The low RH stage corresponds to the period after 4th Dec with daily maximum and minimum RH below 70% and 30%, which was represented by two events that occurred during 9th Dec to 11th Dec (Event 3) and 13th Dec to 15th Dec (Event 4), respectively. These events were selected based on the similarity of $PM_{2.5}$ concentration and evolution, while the time window was fixed to two days for the convenience of intercomparing. In addition, during these events, the wind speed was generally low, the RH followed a general diurnal variations and SA mass grew steadily and continuously. Thus the interference of the variations of air mass and short-term local emissions can be eliminated and the influence of SA formation can be highlighted. It should be noted that variations of N_{CCN} at 0.07% were similar to those at 0.05%, which followed the variations of SA mass concentration. While at higher SSs, the variations of N_{CCN} differed from those of SA mass concentration, especially under high RH conditions, suggesting different responses of CCN activity towards distinct SA formation processes. As reported in Kuang et al. (2020c), during the high RH stage aqueous phase SA formation was promoted, leading to persistent increases in N_{CCN}, mass concentration of NR-$PM_{2.5}$ and especially mass concentration of $PM_{2.5}$ SA during Event 1 and 2. During the low RH stage, the SA formation dominantly occurred in the gas-phase, that generated much less SA than aqueous-phase formation (Kuang et al., 2020c). Thus, the persistent increases of N_{CCN} and $PM_{2.5}$ during Event 3 and

320   4 was much weaker than those in Events 1 and 2. Due to the different SA mass fractions, SPAR during

321   the high RH stage was generally higher than that during the low RH stage. However, the ratios between

322   N_{CCN} and mass concentration of $PM_{2.5}$ SA or NR-$PM_{2.5}$, were lower during the high RH period and

323   demonstrated strong decreases, especially in Event 1 and 2. The response of CCN activity and N_{CCN}

324   to the different SA formation mechanisms will be discussed comprehensively in the following parts.

325   **3.2. The influence of different secondary aerosol formation on the diurnal variation of CCN**

326   **activity**

327   The diurnal averages of PNSD, SPAR at SS of 0.05%, GF-PDF for 200 nm particle and mass

328   fraction of particle chemical compositions during high RH periods before 4th Dec, low RH periods

329   after 4th Dec and the four events are shown in Fig. 2, respectively. To be noted, the "high (or low) RH

330   events" is used to refer to the SA formation events under high (or low) RH conditions for convivence,

331   and it doesn't mean that RH caused variations of CCN behavior. As can be seen in Figs. 2 (1b) and

332   (2b), different variations of SPAR due to SA formations can be found during the periods with different

333   RH conditions. The average diurnal variations of these parameters for the entire high RH stage and

334   low RH stage as shown in Figs. 2 (1a-1d) and (2a-2d) revealed similar but more smoothed variations

335   as in the four selected events. The four events are discussed and intercompared in the following to

336   magnify the differences under distinct RH conditions. For accumulation mode particles, particle

337   number concentrations were higher during daytime in high RH events, while stronger diurnal

338   variations occurred in low RH events. Simultaneous daytime increases in particle SPAR,

339   hygroscopicity and SA mass fraction were found in all four events, suggesting that SA formation led

340   to increasing hygroscopic particles number concentration, which in turn enhanced particle CCN

341   activity. This effect was more pronounced in Events 1 and 2 than in Events 3 and 4. In Events 1 and

342   2, SPAR values were generally higher than 0.4 at 200 nm and reached the maximum of 1 during

343   noontime at 300 nm. A hygroscopic mode with GF>1.4 was be found throughout the day, which

344   dominated aerosol hygroscopicity during daytime. Mass fraction of SA were generally higher than 70%

345   and reach a maximum of 80% at noon. While in Events 3 and 4, SPAR at 200 nm was lower than 0.4

346   at night and the maximum SPAR at 300 nm was lower than 0.9. A particle mode with GF<1.1

347   dominates particle hygroscopicity, and the mass fraction of SA was lower than 60% and 30% at noon

348   and at night, respectively. However, stronger daytime increase of SA mass fraction and accordingly

349   larger variation in SPAR was observed in Events 3 and 4 than in Events 1 and 2.

350   Besides SS of 0.05%, variations of SPAR at SSs of 0.07% and 0.2% are also shown in Figs.

351   S1 and S2 in the supplement. And as shown in Figs. S1 and S2, the variations of SPAR and N_{CCN}/PM

352   at SS of 0.07% are similar but lighter, compared with those at SS of 0.05%. While for SS of 0.2%, the

353   difference of SPAR between different periods or events are smaller (Fig. S1), and so did the diurnal

354   variations of SPAR and GF-PDF at particle size of 100nm (Fig. S2). Because CCN activity at SS of

355   0.2% was strong enough (indicated by SPAR value close to 1) in particle size range where the SA

356   formation dominates, and thus the different SA formations under high or low RH conditions cannot

357   lead to significant variations of CCN activity at SS of 0.2%. In summary, based on CCN measurements

358   in this study, the RH-dependent influence of SA formation on CCN activity can be found obviously at

359   SSs of 0.05% and 0.07%. As the variations of SPAR at SS of 0.07% were quite similar to those at SS

360   of 0.05%, further analysis was only based on CCN activity at SS of 0.05%.

361   In Fig. 3a, detailed comparison of particle CCN activity during SA formation events of N_{CCN}

362   enhancements at SS of 0.05% under different RH conditions are shown as the variations of SPAR

363   curves. Particle CCN activity in Events 1 and 2 were combined due to their similar diurnal variations

364   (as shown in Fig. 2). Besides SPAR curves (Fig. 3a), corresponding fitting parameters of the SPAR

365   curve including D_a and MAF were also shown in Figs. 3b and c, respectively, as enhanced SPAR for

366   particle population can be attributed to hygroscopic particle number fraction increase (MAF increase)

367   or enhancement of hygroscopic particle hygroscopicity (D_a decrease). Same as demonstrated in Fig. 2,

368   SPAR was generally higher and thus particle CCN activity were generally stronger in high RH events

369   than those in low RH events. However, as shown in Fig. 3a, the difference between SPAR in high and

370   low RH events at 300 nm decreased from 0.2 to 0.1 during the SA formations, indicating for a stronger

371   enhancement in low RH events, probably due to both the stronger increase of SA mass fraction and

372   the higher nighttime PA mass fraction (Fig. 2(e)). Furthermore, in high RH events, there were daytime

373   enhancements of SPAR within the 150 to 300 nm size range, as was indicated by the daytime increase

374   of MAF and decrease of Da, which mainly resulted from number fraction and hygroscopicity increases

375   of CCN-active particles. While in low RH events, the daytime enhancement of SPAR was only

376   observed for particles larger than 200 nm. This can be attributed to the strong increase of MAF and

377   the slight decrease of D_a, which indicates significant increasing number fraction yet slightly enhanced

378   hygroscopicity of hygroscopic particles, respectively. Overall, the enhancement of SPAR was weaker

379   but occurred at a broader particle size range in high RH events than in low RH events, as shown in Fig.

380   3a. This is in accordance with previous the results from Kuang et al. (2020c), suggesting that SA

381   formation occurred mainly in aqueous phase within a broad particle size range (up to 1 μm) in high

382   RH events, while SA formation dominantly proceeded via gas phase reactions and contributed to

383   aerosol sizes smaller than 300 nm in low RH events. At SS of 0.05% (Fig. 3(a)), the variation of SPAR

384   from 8:00-12:00 to 12:00-16:00 in particle size smaller than 200 nm was very small during low RH

385 events, suggesting a smaller CCN activity enhancement due to SA formation compared with those at
386 high RH events.

387 As there were different influences of SA formation on both CCN activity at SS of 0.05% and
388 PNSD under different RH conditions, different variation of N_{CCN} due to SA formation can also be
389 expected. Fig. 4 displays the diurnal variation of $PM_{2.5}$ mass concentration, volume concentration
390 (Vconc) , number concentration (Nconc) and N_{CCN} (all divided by CO to partially compensate for
391 changes in planetary boundary layer height), as well as the $N_{CCN}/PM_{2.5}$ mass concentration ratio and
392 SPAR during high and low RH events, respectively. Variables in Fig. 4 were also presented in Fig. S3
393 averaged for the entire high RH and low RH stages, respectively. Compared with the selected case
394 events featuring significant N_{CCN} enhancement (Fig. 4(1c-2c)), the diurnal variations averaged for the
395 entire high and low RH stages were similar, with higher levels of particle mass concentration but
396 weaker enhancement of SA and N_{CCN}, indicating similar but weakened impact of SA formation on
397 CCN activity due to the interference of other aerosol processes. Hereinafter, we discuss the variations
398 in the four events to magnify the discrepancies of SA formation under high RH and low RH conditions
399 and its distinct impact on N_{CCN}. The Vconc size distribution variations can be used as a proxy for the
400 evolution of NR-$PM_{2.5}$ size distributions, considering the relatively small variations in particle density
401 (ranging from 1.2 to 1.8 and with relative variations within 20% (Hu et al., 2012; Zhao et al., 2019)).
402 The variations of the ratio between N_{CCN} (in different particle size range) and the mass concentration
403 of $PM_{2.5}$ SA (referred as to N_{CCN}/SA) or NR-$PM_{2.5}$ (referred as to N_{CCN}/NR) can be used to evaluate
404 the response of N_{CCN} to SA formation.

405 During high RH events, normalized N_{CCN} increased by ~ 50% from 8:00 to 14:00, with a similar
406 increase in normalized $PM_{2.5}$ SA mass concentration (Fig. 4(1a)). As the $PM_{2.5}$ PA mass concentration
407 decrease was much smaller than the SA increase, the NR-$PM_{2.5}$ mass concentration increase can be
408 expected to be similar to the SA increase. As reported by Kuang et al. (2020c), SA during daytime
409 were mainly formed at larger particle sizes, featuring Vconc increase in the particle size range of 400 to
410 1000 nm. In Fig. 4(1d), significant increases of particle number concentration (Nconc) in particle size
411 range of 150nm to 1000 nm can be observed. At larger particle size the increase of Nconc led to
412 stronger increase of Vconc, which is why there was simultaneous but much weaker increases of Vconc
413 in particle size range of 150 to 300 nm compared with increases of those in particle size of larger than
414 300 nm (Fig. 4(1b)). This suggests that $PM_{2.5}$ SA mainly contributed to particle sizes of larger than
415 300 nm. In addition, because the SA formation enhanced hygroscopicity and number fraction of CCN-
416 active particles in particle size range of 150 to 300 nm, simultaneous enhancements of SPAR can be
417 found throughout the measured particle size range of 180 to 300 nm (Fig. 4(1e)). By combining the

enhancements of Nconc and SPAR in measured particle size ranges, there were increases of N_{CCN} from 200 to 500 nm (Fig. 4(1c)). While the strongest Vconc increases occurred at particle sizes larger than 300 nm, the N_{CCN} increased most in the particle size range of 200 to 300 nm, suggesting that particles larger than 300 nm were already CCN-active before SA formation. Thus while SA formation processes contributed to their volume (mass) and hygroscopicity increase, it had no further impact on N_{CCN}. As a result, N_{CCN} (>300 nm)/SA, N_{CCN} (<300 nm)/SA, N_{CCN} (>300 nm)/NR and N_{CCN} (<300 nm)/NR all decreased during the SA formation (Fig. 4(1f)), suggesting that weakening enhancement of N_{CCN} in SA formation under high RH condition as SA formation mainly added mass to already CCN-active particles .

During low RH events, weaker increases of both N_{CCN} and $PM_{2.5}$ SA mass concentration from 8:00 to 14:00 was found (Fig. 4(2a)). At the same time, PA mass decreased by 50% and the variation of total NR mass was small. Under low RH conditions, SA formation mainly contributed to mass enhancements of smaller particle sizes (Kuang et al., 2020c). Vconc increased mostly in the range of 150 to 300 nm (Fig. 4(2b)), while Nconc only increased within 300 nm (Fig. 4(2d)), suggesting that $PM_{2.5}$ SA mainly formed in particle size range within 300 nm. SA formation mainly enhanced number fraction of CCN-active particles in particle size of 200 to 300 nm, as SPAR only revealed evident enhancement (Fig. 4(2e)) and N_{CCN} only significantly increased (Fig. 4(2c)) in that size range. As a result, although N_{CCN} (>300 nm)/SA decreased similar as that under high RH conditions, N_{CCN} (<300 nm)/SA and N_{CCN} (>300 nm)/NR generally stayed constant and N_{CCN} (<300 nm)/NR even increased during SA formation in daytime (Fig. 4(2f)). The ratio between bulk N_{CCN} and mass concentration of NR-$PM_{2.5}$ became larger due to the SA formation, suggesting that stronger enhancement of N_{CCN} in SA formation under low RH condition, because SA formation mainly added mass to CCN-inactive particles and turned them into CCN-active particles.

In summary, during the campaign in this study, two kinds of SA formation events were observed under different RH conditions with different variations of PM and N_{CCN} at SSs lower than 0.07%. Under high RH conditions, there were strong SIA dominated SA formation leading to higher particle hygroscopicity and N_{CCN} enhancements. Meanwhile, under low RH conditions, there were moderate SOA dominated SA formation with moderate particle hygroscopicity and N_{CCN} enhancements. However, for a unit amount of SA formation, the increase of N_{CCN} was stronger under low RH conditions and weaker under high RH conditions. This was because SA formation under low RH conditions was more concentrated on particle sizes smaller than 300 nm and added more mass to CCN-inactive particles, turning them into CCN-active particles. In addition, strong and distinct diurnal

450 variations of CCN activity of particles were observed during different SA formation processes, whose

451 effects on N_{CCN} calculation need to be further evaluated.

452

3.3. The influence of diurnal variation of CCN activity on N_{CCN} prediction

454   Since PNSD measurements are generally more simple and common than N_{CCN} measurement,

455 N_{CCN} is usually estimated from real-time PNSD combined with parameterized CCN activity. In former

456 sections, it was already manifested that SA formations under different RH conditions led to distinct

457 variations in PNSD and SPAR at SS of 0.05%, thus different variations in N_{CCN}. Thus, it is important

458 for the prediction of N_{CCN} to quantify its sensitivity towards changes in PNSD and SPAR during SA

459 formation processes under different RH conditions.

460   In this study, PNSD dominated the N_{CCN} calculation as was generally found in former studies

461 (Dusek et al., 2006), but the variation of CCN activity also contributed significantly to the deviation

462 of N_{CCN} calculation during SA formation. In former discussions, CCN activity (indicated by SPAR) at

463 0.05% SS revealed significant diurnal variations during this campaign, which were different during

464 SA formations under distinct RH conditions. The ratio between N_{CCN} calculated based on campaign

465 averaged SPAR (N_{CCN_cal}) to measured N_{CCN} (N_{CCN_meas}) at 0.05% SS before and after 4th Dec are

466 shown in Fig. 5. SPAR is determined by the variation of D_a and MAF, which reflect changes in

467 hygroscopicity and number fraction of hygroscopic particles. Thus, to investigate the separate

468 influence of MAF and D_a variations on N_{CCN} predictions, N_{CCN_AvgMAF} (or N_{CCN_avgDa}) was calculated

469 based on the real-time PNSD and SPAR estimated by replacing MAF (or D_a) in Eq. 7 with the

470 campaign averaged value. During the high RH stage, underestimation of daytime N_{CCN_cal} can reach

471 up to 20%, since SPAR variations due to CCN activity enhancement were not considered. Similar

472 deviations of both N_{CCN_AvgMAF} and N_{CCN_avgDa} from N_{CCN_meas} were detected, suggesting that both

473 MAF and D_a variations contributed to N_{CCN_cal} underestimation under high RH conditions. During the

474 low RH stage, up to 50% overestimation existed in $N_{CCN\_AvgSPAR}$ beyond SA formation episodes. Only

475 N_{CCN_AvgMAF} displayed similar deviations from N_{CCN_meas}, indicating that differences between N_{CCN_cal}

476 and N_{CCN_meas} were mainly contributed by variations in MAF brought on by significant CCN-active

477 particles number fraction growth due to SA formations. To be noted, $N_{CCN\_AvgSPAR}$ before and after 4th

478 Dec are both on the basis of the averaged SPAR of this campaign (green dots in Fig. 5a) rather than

479 the averaged SPAR before or after 4th, because the applicability of the campaign averaged SPAR on

480 the N_{CCN} calculation in the NCP was confirmed in many former studies (Deng et al., 2012; Wang et

481 al., 2013; Ma et al., 2016). During the low RH periods, SPAR are generally lower than the averaged

482 SPAR of the campaign and the ratio between the calculated and measured N_{CCN} are systematically

483 higher (lasting for the whole night). In summary, SA formation processes can induce significant

484 deviation to N_{CCN} prediction, which mainly resulted from the variation of MAF and also varied under

485 different RH conditions. Thus, for accurate N_{CCN} estimations, considering the variation of MAF

486 (changes in aerosol hygroscopicity) is highly essential.

487   As SOA is generally considered to be more hygroscopic than POA (Frosch et al., 2011; Lambe

488 et al., 2011; Kuang et al., 2020a), the increase of hygroscopic particles or SA particles (both SIA and

489 SOA) were considered to be the cause for the increase of SPAR within 200 to 300 nm size range (Fig.

490 2). In order to account for the variations of hygroscopic particles or SA particles in N_{CCN} calculation,

491 Number Fraction of hygroscopic particles (GF(90%, 200 nm)>1.22, NF_{hygro}) measured by HTDMA

492 and Mass Fraction of SA particles (MF_{SA}) measured by ACSM were used to represent MAF variations

493 and to provide calculation of N_{CCN} at SS of 0.05% combining with PNSD measurement with smaller

494 deviations.

495   Based on the bulk hygroscopicity derived from particle chemical compositions measurements

496 (κ_{chem}), a critical diameter can be calculated based on κ-Köhler theory and based on which N_{CCN} can

497 be predicted by combining measured PNSD with this critical diameter (N_{CCN_Chem}). Although there

498 can be significant deviations for κ of accumulation mode particles derived from chemical composition

499 of the bulk aerosol, which leads to significant deviations of N_{CCN} prediction. However, in practice, the

500 measurements of chemical compositions of accumulation mode particles are not common, and

501 chemical composition of the bulk aerosol is still commonly applied in CCN studies (Zhang et al., 2014;

502 Zhang et al., 2016; Che et al., 2017; Cai et al., 2018), especially when particle hygroscopicity

503 measurements were in lack. In Fig. 6(a), it can be found that N_{CCN_meas} at 0.05% SS can be strongly

504 underestimated by N_{CCN_Chem}, especially at lower N_{CCN_meas} ($\sim10^2$ # cm^{-3}), which is similar to results

505 of studies that encountered high fractions of organics (Chang et al., 2010; Kawana et al., 2015). This

506 deviation between N_{CCN_meas} and N_{CCN_Chem} may have resulted from the hypothesis of internal mixing

507 state and the difference of particle hygroscopicity derived by particle chemical composition

508 measurements and CCN activity. Fig. 6(b) depicts the correlation between mass fraction of SA (MF_{SA})

509 and MAF at 0.05% SS. MF_{SA} was generally positively correlated to MAF (r=0.8) with slight

510 underestimations, suggesting that externally mixed SA dominated CCN-active particles. Thus, in the

511 prediction of N_{CCN}, real-time SPAR can be calculated from average D_a and MAF assumed to equal to

512 real-time MF_{SA} (N_{CCN_MF}). As displayed in Fig. 6(c), the underestimation and correlation between

513 N_{CCN_cal} and N_{CCN_meas} was improved after introducing MF_{SA} into N_{CCN} calculation. Additionally, the

514 diurnal variations of N_{CCN_cal}/N_{CCN_meas} ratio based on different methods of N_{CCN} calculation during

the whole campaign were shown in Fig. 6(d). It can be found that by considering the real-time MF_{SA}, the deviation of calculated N_{CCN} (Real-time MF) can be reduced throughout the day, compared with N_{CCN_Chem} (Real-time Chem). Meanwhile, if an averaged MF_{SA} is used to estimate SPAR and N_{CCN}, the deviations of calculated N_{CCN} (Averaged MF) can be reduced as well, but demonstrated a much stronger diurnal variations than the deviation of N_{CCN_MF}.

Based on the bulk hygroscopicity derived from GF measurement (κ_{GF}) at 200 nm, a critical diameter can be calculated based on κ-Köhler theory and N_{CCN} at 0.05% SS can be predicted by combining measured PNSD and the critical diameter (N_{CCN_GF}). Fig. 7(a) shows that N_{CCN_meas} were strongly underestimated by N_{CCN_GF} (by more than 30%). This deviation may also have result from the hypothesis of internal mixing state and the difference of particle hygroscopicity derived by GF and particle CCN activity measured under different water vapor saturated conditions. Fig. 7(b) depicts the positive correlation between NF_{hygro} and MAF at 0.05% SS, which was weaker than that between MF_{SA} and MAF. Similar as before, NF_{hygro} was applied as a proxy for MAF in the N_{CCN} calculation, which also improved the underestimation and correlation between N_{CCN_cal} and N_{CCN_meas} (Fig. 7(c)). The diurnal variations of the N_{CCN_cal}/N_{CCN_meas} ratio based on different methods of N_{CCN} calculation during the whole campaign were shown in Fig. 7(d). It can be found that by considering the real-time NF_{hygro}, the deviation of N_{CCN_NF} (Real-time NF) can be reduced mainly during nighttime, compared with N_{CCN_GF} (Real-time GF). Meanwhile, if an averaged NF_{hygro} is used to estimate SPAR and N_{CCN}, the deviations of calculated N_{CCN} (Averaged NF) can be reduced during nighttime as well, but demonstrated a stronger diurnal variations than the deviation of N_{CCN_NF}. If GF-PDF were directly used to calculate N_{CCN}, N_{CCN_cal} would agree well with measured N_{CCN} (Fig. S4), because in this way the mixing state of aerosol would have been accounted for. However, compared to the approach using GF-PDF, NF_{hygro} is easier to apply in N_{CCN} calculation and can yield similar accuracies.

In summary, MAF exhibited strong diurnal variation that varied under different RH conditions due to different SA formation mechanisms, which contributed most to N_{CCN} estimation deviations if unaccounted for. The diurnal variations of MAF at the five measured SSs (Fig. S5) reveal significant diurnal variations in MAF at low SSs (0.05% and 0.07%) that are dependent on RH conditions, while small diurnal variations that are insensitive to the RH conditions at SSs over 0.2%. In general, MAF become lower at lower SSs, especially during nighttime. As the fraction of CCN-active particles were generally hygroscopic and composed of secondary compounds, positive correlation was found between MAF, MF_{SA} and NF_{hygro}. Although a good prediction of N_{CCN} was achieved by applying an averaged MAF (Figs. 5, 6d and 7d), in practice, this would still require CCN measurements or HTDMA/chemical composition measurements as proxies. Additionally, deviations of N_{CCN_cal} based

548 on the averaged MAF can be large under low RH conditions (Fig. 5c), while time-dependent MAF can

549 eliminate a great part of these deviations. Thus, by replacing MAF with real-time MF_{SA} or NF_{hygro}

550 when deriving SPAR curve, the relative deviation of N_{CCN} calculation can be reduced. The proposed

551 N_{CCN} parameterization using MF_{SA} can also be easily adopted by chemical-transport and climate

552 models, improving their representation of N_{CCN} changes due to distinct SA formation processes.

553

4. Conclusions

SA formation drives the development of haze pollution in the NCP and can result in significant variations of PNSD and aerosol hygroscopicity. Studies in the NCP have shown that the mechanism of SA formation can be affected by relative humidity (RH), and thus has different influences on the aerosol hygroscopicity and PNSD under distinct RH conditions. The difference in particle size where SA formation is taking place and the different chemical compositions of formed SA can result in different variations of CCN activity. Thus, it is essential to study the influence of SA formation on CCN activity of existing accumulation mode particles under different RH conditions in the NCP. As N_{CCN} is often predicted based on real-time PNSD and parameterized SPAR, the influence of varying SPAR in distinct SA formation processes on N_{CCN} calculation needs to be evaluated in detail.

Based on the measurements of CCN-activity, particle hygroscopicity, particle chemical composition, PNSD during the McFAN campaign in Gucheng winter 2018, the influences of SA formation on CCN activity and N_{CCN} calculation under different RH conditions were investigated especially at SSs lower than 0.07%. Two kinds of SA formation events were identified under different RH conditions with distinct variations in PM and N_{CCN} at 0.05% SS. Under high RH conditions, which corresponds to the periods with minimum RH higher than 50% in daytime, strong SA formation and N_{CCN} enhancements with strong hygroscopic particles and SIA dominated contribution to SA (>70%) was found. While under low RH conditions, which corresponds to the periods with daytime minimum RH below 30%, moderate SA formation and N_{CCN} enhancements with moderately hygroscopic particles and SOA dominated contribution to SA was found. However, the increase of N_{CCN} under the a same amount of SA formation was stronger under low RH conditions and weaker under high RH conditions. This was because the formation of SA under low RH conditions was more concentrated in particle size range smaller than 300 nm and added more mass to CCN-inactive particles turning them into CCN-active ones after SA formation.

In addition, strong diurnal variations of CCN activity of particles at 0.05% SS due to the strong SA formations were also observed, both varying with RH conditions. N_{CCN} was significantly underestimated when MAF (SPAR parameter) variations were not considered. As the fraction of CCN-active particles were generally hygroscopic and composed of secondary compounds, there were good correlation among MAF inferred from measurements of CCN activity, particle hygroscopicity and particle chemical compositions. Thus, the relative deviation of N_{CCN} estimation can be reduced by applying measurements of particle hygroscopicity or particle chemical compositions as a proxy for aerosol mixing state.

586   This study can further the understanding of the impact of SA formation on CCN activity and
587 N$_{CCN}$ calculation, specifically for SA formations on existing particles, which can strongly affect cloud
588 microphysics properties in stratus clouds and fogs. The investigation of the influence of SA formation
589 on CCN activity of existing particles in this study is important for improving N$_{CCN}$ parameterizations
590 in chemical-transport and climate models, so that they can account for the large variations induced by
591 SA formation processes.

592

593 Supporting Information

594 The supporting information is available in a separate file.

595 Data availability.

596 The data used in this study are available from the corresponding author upon request
597 (taojch@jnu.edu.cn and nan.ma@ jnu.edu.cn)

598 Author contributions.

599 JT, YK and NM designed this research. JT performed the data analysis and wrote the manuscript. YC,
600 HS, NM, YK, JT, and JH planned this campaign. JT and YZ conducted the CCN measurements. YS
601 and YH conducted the ACSM measurements and the ACSM PMF analysis. JH and QL conducted the
602 HTDMA measurements. LX and YZ conducted the particle number size distribution measurements.
603 WX conducted the measurements of CO and meteorological parameters. YC, HS, YS, YK and NM
604 contributed to the revisions of this manuscript and all other coauthors have contributed to this paper in
605 different ways.

606 Acknowledgement

607 We acknowledge the National Key Research and Development Program of China (grant no.
608 2017YFC0210104), the National Natural Science Foundation of China (grant no. 91644218 and
609 41805110), the Guangdong Innovative and Entrepreneurial Research Team Program (Research team
610 on atmospheric environmental roles and effects of carbonaceous species: 2016ZT06N263), Special
611 Fund Project for Science and Technology Innovation Strategy of Guangdong Province
612 (2019B121205004) and the Basic Research Fund of CAMS (2020Z002)..

613 Conflicts of interest

614   There are no conflicts to declare.

615

616

Reference:

Cai, M., Tan, H., Chan, C. K., Qin, Y., Xu, H., Li, F., Schurman, M. I., Liu, L., and Zhao, J.: The size-resolved cloud condensation nuclei (CCN) activity and its prediction based on aerosol hygroscopicity and composition in the Pearl Delta River (PRD) region during wintertime 2014, Atmos. Chem. Phys., 18, 16419–16437, https://doi.org/10.5194/acp-18-16419-2018, 2018.

Chang, R. Y.-W., Slowik, J. G., Shantz, N. C., Vlasenko, A., Liggio, J., Sjostedt, S. J., Leaitch, W. R., and Abbatt, J. P. D.: The hygroscopicity parameter (κ) of ambient organic aerosol at a field site subject to biogenic and anthropogenic influences: relationship to degree of aerosol oxidation, Atmos. Chem. Phys., 10, 5047–5064, https://doi.org/10.5194/acp-10-5047-2010, 2010.

Che, H., Zhang, X., Zhang, L., Wang, Y., Zhang, Y., Shen, X., Ma, Q., Sun, J., and Zhong, J.: Prediction of size-resolved number concentration of cloud condensation nuclei and long-term measurements of their activation characteristics, Scientific reports, 7, 1–12, 2017.

Cheng, Y. F., Su, H., Rose, D., Gunthe, S. S., Berghof, M., Wehner, B., Achtert, P., Nowak, A., Takegawa, N., Kondo, Y., Shiraiwa, M., Gong, Y. G., Shao, M., Hu, M., Zhu, T., Zhang, Y. H., Carmichael, G. R., Wiedensohler, A., Andreae, M. O., and Pöschl, U.: Size-resolved measurement of the mixing state of soot in the megacity Beijing, China: diurnal cycle, aging and parameterization, Atmos. Chem. Phys., 12, 4477–4491, https://doi.org/10.5194/acp-12-4477-2012, 2012.

Dal Maso, M., Kulmala, M., Riipinen, I., Wagner, R., Hussein, T., Aalto, P. P., and Lehtinen, K. E. J.: Formation and growth of fresh atmospheric aerosols: eight years of aerosol size distribution data from SMEAR II, Hyytiala, Finland, 10, 323–336, 2005.

Deng, Z. Z., Zhao, C. S., Ma, N., Liu, P. F., Ran, L., Xu, W. Y., Chen, J., Liang, Z., Liang, S., Huang, M. Y., Ma, X. C., Zhang, Q., Quan, J. N., Yan, P., Henning, S., Mildenberger, K., Sommerhage, E., Schäfer, M., Stratmann, F., and Wiedensohler, A.: Size-resolved and bulk activation properties of aerosols in the North China Plain, Atmos. Chem. Phys., 11, 3835–3846, https://doi.org/10.5194/acp-11-3835-2011, 2011.

Deng, Z. Z., Zhao, C. S., Ma, N., Ran, L., Zhou, G. Q., Lu, D. R., and Zhou, X. J.: An examination of parameterizations for the CCN number concentration based on in situ measurements of aerosol activation properties in the North China Plain, Atmos. Chem. Phys., 13, 6227–6237, https://doi.org/10.5194/acp-13-6227-2013, 2013.

646 Ditas, F., Shaw, R. A., Siebert, H., Simmel, M., Wehner, B., and Wiedensohler, A.: Aerosols-cloud
647 microphysics-thermodynamics-turbulence: evaluating supersaturation in a marine stratocumulus cloud,
648 Atmos. Chem. Phys., 12, 2459–2468, https://doi.org/10.5194/acp-12-2459-2012, 2012.

649 Duan, J., Wang, Y., Xie, X., Li, M., Tao, J., Wu, Y., Cheng, T., Zhang, R., Liu, Y., Li, X., He, Q.,
650 Gao, W., and Wang, J.: Influence of pollutants on activity of aerosol cloud condensation nuclei (CCN)
651 during pollution and post-rain periods in Guangzhou, southern China, 642, 1008–1019,
652 https://doi.org/10.1016/j.scitotenv.2018.06.053, 2018.

653 Dusek, U., Frank, G., Hildebrandt, L., Curtius, J., Schneider, J., Walter, S., Chand, D., Drewnick, F.,
654 Hings, S., and Jung, D.: Size matters more than chemistry for cloud-nucleating ability of aerosol
655 particles, Science, 312, 1375–1378, 2006.

656 Fan, J., Wang, Y., Rosenfeld, D., and Liu, X.: Review of Aerosol–Cloud Interactions: Mechanisms,
657 Significance, and Challenges, Journal of the Atmospheric Sciences, 73, 4221–4252,
658 https://doi.org/10.1175/JAS-D-16-0037.1, 2016.

659 Farmer, D. K., Cappa, C. D., and Kreidenweis, S. M.: Atmospheric Processes and Their Controlling
660 Influence on Cloud Condensation Nuclei Activity, 115, 4199–4217,
661 https://doi.org/10.1021/cr5006292, 2015.

662 Frosch, M., Bilde, M., DeCarlo, P., Jurányi, Z., Tritscher, T., Dommen, J., Donahue, N., Gysel, M.,
663 Weingartner, E., and Baltensperger, U.: Relating cloud condensation nuclei activity and oxidation
664 level of α-pinene secondary organic aerosols, Journal of Geophysical Research: Atmospheres, 116,
665 2011.

666 Gordon, H., Sengupta, K., Rap, A., Duplissy, J., Frege, C., Williamson, C., Heinritzi, M., Simon, M.,
667 Yan, C., Almeida, J., Trostl, J., Nieminen, T., Ortega, I. K., Wagner, R., Dunne, E. M., Adamov, A.,
668 Amorim, A., Bernhammer, A.-K., Bianchi, F., Breitenlechner, M., Brilke, S., Chen, X., Craven, J. S.,
669 Dias, A., Ehrhart, S., Fischer, L., Flagan, R. C., Franchin, A., Fuchs, C., Guida, R., Hakala, J., Hoyle,
670 C. R., Jokinen, T., Junninen, H., Kangasluoma, J., Kim, J., Kirkby, J., Krapf, M., Kuerten, A.,
671 Laaksonen, A., Lehtipalo, K., Makhmutov, V., Mathot, S., Molteni, U., Monks, S. A., Onnela, A.,
672 Perakyla, O., Piel, F., Petaja, T., Praplan, A. P., Pringle, K. J., Richards, N. A. D., Rissanen, M. P.,
673 Rondo, L., Sarnela, N., Schobesberger, S., Scott, C. E., Seinfeldo, J. H., Sharma, S., Sipila, M., Steiner,
674 G., Stozhkov, Y., Stratmann, F., Tome, A., Virtanen, A., Vogel, A. L., Wagner, A. C., Wagner, P. E.,
675 Weingartner, E., Wimmer, D., Winkler, P. M., Ye, P., Zhang, X., Hansel, A., Dommen, J., Donahue,
676 N. M., Worsnop, D. R., Baltensperger, U., Kulmala, M., Curtius, J., and Carslaw, K. S.: Reduced

anthropogenic aerosol radiative forcing caused by biogenic new particle formation, 113, 12053–12058, https://doi.org/10.1073/pnas.1602360113, 2016.

Gryspeerdt, E. and Stier, P.: Regime-based analysis of aerosol-cloud interactions, Geophysical Research Letters, 39, https://doi.org/10.1029/2012GL053221, 2012.

Gysel, M., Crosier, J., Topping, D. O., Whitehead, J. D., Bower, K. N., Cubison, M. J., Williams, P. I., Flynn, M. J., McFiggans, G. B., and Coe, H.: Closure study between chemical composition and hygroscopic growth of aerosol particles during TORCH2, Atmos. Chem. Phys., 7, 6131–6144, https://doi.org/10.5194/acp-7-6131-2007, 2007.

Gysel, M., McFiggans, G. B., and Coe, H.: Inversion of tandem differential mobility analyser (TDMA) measurements, 40, 134–151, https://doi.org/10.1016/j.jaerosci.2008.07.013, 2009.

Hagen, D. E. and Alofs, D. J.: Linear Inversion Method to Obtain Aerosol Size Distributions from Measurements with a Differential Mobility Analyzer, Aerosol Science and Technology, 2, 465–475, https://doi.org/10.1080/02786828308958650, 1983.

Hammer, E., Bukowiecki, N., Gysel, M., Jurányi, Z., Hoyle, C. R., Vogt, R., Baltensperger, U., and Weingartner, E.: Investigation of the effective peak supersaturation for liquid-phase clouds at the high-alpine site Jungfraujoch, Switzerland (3580 m a.s.l.), Atmos. Chem. Phys., 14, 1123–1139, https://doi.org/10.5194/acp-14-1123-2014, 2014a.

Hammer, E., Gysel, M., Roberts, G. C., Elias, T., Hofer, J., Hoyle, C. R., Bukowiecki, N., Dupont, J.-C., Burnet, F., Baltensperger, U., and Weingartner, E.: Size-dependent particle activation properties in fog during the ParisFog 2012/13 field campaign, Atmos. Chem. Phys., 14, 10517–10533, https://doi.org/10.5194/acp-14-10517-2014, 2014b.

Hong, J., Xu, H., Tan, H., Yin, C., and Kerminen, V. M.: Mixing state and particle hygroscopicity of organic-dominated aerosols over the Pearl River Delta region in China, Atmos. Chem. Phys., 18, 14079–14094, 2018.

Hu, M., Peng, J., Sun, K., Yue, D., Guo, S., Wiedensohler, A., and Wu, Z.: Estimation of Size-Resolved Ambient Particle Density Based on the Measurement of Aerosol Number, Mass, and Chemical Size Distributions in the Winter in Beijing, Environ. Sci. Technol., 46, 9941–9947, https://doi.org/10.1021/es204073t, 2012.

Hu, W., Hu, M., Hu, W., Jimenez, J. L., Yuan, B., Chen, W., Wang, M., Wu, Y., Chen, C., Wang, Z., Peng, J., Zeng, L., and Shao, M.: Chemical composition, sources, and aging process of submicron

707 aerosols in Beijing: Contrast between summer and winter, Journal of Geophysical Research:
708 Atmospheres, 121, 1955–1977, https://doi.org/10.1002/2015JD024020, 2016.

709 Hu, W., Campuzano-Jost, P., Day, D. A., Croteau, P., Canagaratna, M. R., Jayne, J. T., Worsnop, D.
710 R., and Jimenez, J. L.: Evaluation of the new capture vapourizer for aerosol mass spectrometers (AMS)
711 through laboratory studies of inorganic species, Atmos. Meas. Tech., 10, 2897–2921,
712 https://doi.org/10.5194/amt-10-2897-2017, 2017a.

713 Hu, W., Hu, M., Hu, W.-W., Zheng, J., Chen, C., Wu, Y., and Guo, S.: Seasonal variations in high
714 time-resolved chemical compositions, sources, and evolution of atmospheric submicron aerosols in
715 the megacity Beijing, Atmos. Chem. Phys., 17, 9979–10000, https://doi.org/10.5194/acp-17-9979-
716 2017, 2017b.

717 Huang, R.-J., Zhang, Y., Bozzetti, C., Ho, K.-F., Cao, J.-J., Han, Y., Daellenbach, K. R., Slowik, J. G.,
718 Platt, S. M., Canonaco, F., Zotter, P., Wolf, R., Pieber, S. M., Bruns, E. A., Crippa, M., Ciarelli, G.,
719 Piazzalunga, A., Schwikowski, M., Abbaszade, G., Schnelle-Kreis, J., Zimmermann, R., An, Z., Szidat,
720 S., Baltensperger, U., Haddad, I. E., and Prévôt, A. S. H.: High secondary aerosol contribution to
721 particulate pollution during haze events in China, Nature, 514, 218–222,
722 https://doi.org/10.1038/nature13774, 2014.

723 Jia, H., Ma, X., Yu, F., Liu, Y., and Yin, Y.: Distinct Impacts of Increased Aerosols on Cloud Droplet
724 Number Concentration of Stratus/Stratocumulus and Cumulus, Geophysical Research Letters, n/a,
725 https://doi.org/10.1029/2019GL085081, 2019.

726 Jiang, X., Tao, J., Kuang, Y., Hong, J., and Ma, N.: Mathematical derivation and physical interpretation
727 of particle size-resolved activation ratio based on particle hygroscopicity distribution: Application on
728 global characterization of CCN activity, Atmospheric Environment, 246, 118137,
729 https://doi.org/10.1016/j.atmosenv.2020.118137, 2021.

730 Kawana, K., Nakayama, T., and Mochida, M.: Hygroscopicity and CCN activity of atmospheric
731 aerosol particles and their relation to organics: Characteristics of urban aerosols in Nagoya, Japan, 121,
732 4100–4121, https://doi.org/10.1002/2015jd023213, 2016.

733 Kerminen, V.-M., Paramonov, M., Anttila, T., Riipinen, I., Fountoukis, C., Korhonen, H., Asmi, E.,
734 Laakso, L., Lihavainen, H., Swietlicki, E., Svenningsson, B., Asmi, A., Pandis, S. N., Kulmala, M.,
735 and Petaja, T.: Cloud condensation nuclei production associated with atmospheric nucleation: a
736 synthesis based on existing literature and new results, 12, 12037–12059, https://doi.org/10.5194/acp-
737 12-12037-2012, 2012.

738 Köhler, H.: The nucleus in and the growth of hygroscopic droplets, 32, 1152–1161, 1936.

739 Krüger, M. L., Mertes, S., Klimach, T., Cheng, Y. F., Su, H., Schneider, J., Andreae, M. O., Pöschl,
740 U., and Rose, D.: Assessment of cloud supersaturation by size-resolved aerosol particle and cloud
741 condensation nuclei (CCN) measurements, Atmos. Meas. Tech., 7, 2615–2629,
742 https://doi.org/10.5194/amt-7-2615-2014, 2014.

743 Kuang, Y., Xu, W., Tao, J., Ma, N., Zhao, C., and Shao, M.: A Review on Laboratory Studies and
744 Field Measurements of Atmospheric Organic Aerosol Hygroscopicity and Its Parameterization Based
745 on Oxidation Levels, Current Pollution Reports, 1–15, 2020a.

746 Kuang, Y., He, Y., Xu, W., Zhao, P., Cheng, Y., Zhao, G., Tao, J., Ma, N., Su, H., Zhang, Y., Sun, J.,
747 Cheng, P., Yang, W., Zhang, S., Wu, C., Sun, Y., and Zhao, C.: Distinct diurnal variation in organic
748 aerosol hygroscopicity and its relationship with oxygenated organic aerosol, Atmos. Chem. Phys., 20,
749 865–880, https://doi.org/10.5194/acp-20-865-2020, 2020b.

750 Kuang, Y., He, Y., Xu, W., Yuan, B., Zhang, G., Ma, Z., Wu, C., Wang, C., Wang, S., Zhang, S., Tao,
751 J., Ma, N., Su, H., Cheng, Y., Shao, M., and Sun, Y.: Photochemical Aqueous-Phase Reactions Induce
752 Rapid Daytime Formation of Oxygenated Organic Aerosol on the North China Plain, 54, 3849–3860,
753 https://doi.org/10.1021/acs.est.9b06836, 2020c.

754 Kulmala, M., Riipinen, I., Sipila, M., Manninen, H. E., Petaja, T., Junninen, H., Dal Maso, M., Mordas,
755 G., Mirme, A., Vana, M., Hirsikko, A., Laakso, L., Harrison, R. M., Hanson, I., Leung, C., Lehtinen,
756 K. E. J., and Kerminen, V.-M.: Toward direct measurement of atmospheric nucleation, 318, 89–92,
757 https://doi.org/10.1126/science.1144124, 2007.

758 Lambe, A. T., Onasch, T. B., Massoli, P., Croasdale, D. R., Wright, J. P., Ahern, A. T., Williams, L.
759 R., Worsnop, D. R., Brune, W. H., and Davidovits, P.: Laboratory studies of the chemical composition
760 and cloud condensation nuclei (CCN) activity of secondary organic aerosol (SOA) and oxidized
761 primary organic aerosol (OPOA), 11, 8913–8928, https://doi.org/10.5194/acp-11-8913-2011, 2011.

762 Li, G., Su, H., Ma, N., Tao, J., Kuang, Y., Wang, Q., Hong, J., Zhang, Y., Kuhn, U., and Zhang, S.:
763 Multiphase chemistry experiment in Fogs and Aerosols in the North China Plain (McFAN): integrated
764 analysis and intensive winter campaign 2018, Faraday Discussions, 2021.

765 Liu, H. J., Zhao, C. S., Nekat, B., Ma, N., Wiedensohler, A., van Pinxteren, D., Spindler, G., Müller,
766 K., and Herrmann, H.: Aerosol hygroscopicity derived from size-segregated chemical composition and
767 its parameterization in the North China Plain, Atmos. Chem. Phys., 14, 2525–2539,
768 https://doi.org/10.5194/acp-14-2525-2014, 2014.

Liu, P. F., Zhao, C. S., Göbel, T., Hallbauer, E., Nowak, A., Ran, L., Xu, W. Y., Deng, Z. Z., Ma, N., and Mildenberger, K.: Hygroscopic properties of aerosol particles at high relative humidity and their diurnal variations in the North China Plain, 11, 3479–3494, 2011.

Liu, Z., Wang, Y., Gu, D., Zhao, C., Huey, L. G., Stickel, R., Liao, J., Shao, M., Zhu, T., Zeng, L., Liu, S.-C., Chang, C.-C., Amoroso, A., and Costabile, F.: Evidence of Reactive Aromatics As a Major Source of Peroxy Acetyl Nitrate over China, Environ. Sci. Technol., 44, 7017–7022, https://doi.org/10.1021/es1007966, 2010.

Ma, N., Zhao, C., Tao, J., Wu, Z., Kecorius, S., Wang, Z., Größ, J., Liu, H., Bian, Y., Kuang, Y., Teich, M., Spindler, G., Müller, K., van Pinxteren, D., Herrmann, H., Hu, M., and Wiedensohler, A.: Variation of CCN activity during new particle formation events in the North China Plain, Atmos. Chem. Phys., 16, 8593–8607, https://doi.org/10.5194/acp-16-8593-2016, 2016.

Mei, F., Hayes, P. L., Ortega, A., Taylor, J. W., Allan, J. D., Gilman, J., Kuster, W., de Gouw, J., Jimenez, J. L., and Wang, J.: Droplet activation properties of organic aerosols observed at an urban site during CalNex-LA, 118, 2903–2917, https://doi.org/10.1002/jgrd.50285, 2013.

Petters, M. D. and Kreidenweis, S. M.: A single parameter representation of hygroscopic growth and cloud condensation nucleus activity, Atmos. Chem. Phys., 7, 1961–1971, 2007.

Reutter, P., Su, H., Trentmann, J., Simmel, M., Rose, D., Gunthe, S. S., Wernli, H., Andreae, M. O., and Pöschl, U.: Aerosol- and updraft-limited regimes of cloud droplet formation: influence of particle number, size and hygroscopicity on the activation of cloud condensation nuclei (CCN), Atmos. Chem. Phys., 9, 7067–7080, https://doi.org/10.5194/acp-9-7067-2009, 2009.

Roberts, G. C. and Nenes, A.: A continuous-flow streamwise thermal-gradient CCN chamber for atmospheric measurements, 39, 206–221, 2005.

Rose, D., Gunthe, S. S., Mikhailov, E., Frank, G. P., Dusek, U., Andreae, M. O., and Pöschl, U.: Calibration and measurement uncertainties of a continuous-flow cloud condensation nuclei counter (DMT-CCNC): CCN activation of ammonium sulfate and sodium chloride aerosol particles in theory and experiment, Atmos. Chem. Phys., 8, 1153–1179, 2008.

Rose, D., Nowak, A., Achtert, P., Wiedensohler, A., Hu, M., Shao, M., Zhang, Y., Andreae, M. O., and Poschl, U.: Cloud condensation nuclei in polluted air and biomass burning smoke near the mega-city Guangzhou, China - Part 1: Size-resolved measurements and implications for the modeling of aerosol particle hygroscopicity and CCN activity, Atmos. Chem. Phys., 10, 3365–3383, 2010.

799   Rose, D., Gunthe, S. S., Su, H., Garland, R. M., Yang, H., Berghof, M., Cheng, Y. F., Wehner, B.,

800   Achtert, P., Nowak, A., Wiedensohler, A., Takegawa, N., Kondo, Y., Hu, M., Zhang, Y., Andreae, M.

801   O., and Poschl, U.: Cloud condensation nuclei in polluted air and biomass burning smoke near the

802   mega-city Guangzhou, China -Part 2: Size-resolved aerosol chemical composition, diurnal cycles, and

803   externally mixed weakly CCN-active soot particles, Atmos. Chem. Phys., 11, 2817–2836,

804   https://doi.org/10.5194/acp-11-2817-2011, 2011.

805   Shen, C., Zhao, C., Ma, N., Tao, J., Zhao, G., Yu, Y., and Kuang, Y.: Method to Estimate Water Vapor

806   Supersaturation in the Ambient Activation Process Using Aerosol and Droplet Measurement Data,

807   Journal   of   Geophysical   Research: Atmospheres,   123,   10,606-10,619,

808   https://doi.org/10.1029/2018JD028315, 2018.

809   Su, H., Rose, D., Cheng, Y. F., Gunthe, S. S., Massling, A., Stock, M., Wiedensohler, A., Andreae, M.

810   O., and Poschl, U.: Hygroscopicity distribution concept for measurement data analysis and modeling

811   of aerosol particle mixing state with regard to hygroscopic growth and CCN activation, Atmos. Chem.

812   Phys., 10, 7489–7503, https://doi.org/10.5194/acp-10-7489-2010, 2010.

813   Sun, Y., He, Y., Kuang, Y., Xu, W., Song, S., Ma, N., Tao, J., Cheng, P., Wu, C., Su, H., Cheng, Y.,

814   Xie, C., Chen, C., Lei, L., Qiu, Y., Fu, P., Croteau, P., and Worsnop, D. R.: Chemical Differences

815   Between PM1 and PM2.5 in Highly Polluted Environment and Implications in Air Pollution Studies,

816   47, e2019GL086288, https://doi.org/10.1029/2019GL086288, 2020.

817   Tan, H., Xu, H., Wan, Q., Li, F., Deng, X., Chan, P. W., Xia, D., and Yin, Y.: Design and Application

818   of an Unattended Multifunctional H-TDMA System, 30, 1136–1148, https://doi.org/10.1175/JTECH-

819   D-12-00129.1, 2013.

820   Tao, J., Kuang, Y., Ma, N., Zheng, Y., Wiedensohler, A., and Zhao, C.: An improved parameterization

821   scheme for size-resolved particle activation ratio and its application on comparison study of particle

822   hygroscopicity   measurements   between   HTDMA   and   DMA-CCNC,   226,   117403,

823   https://doi.org/10.1016/j.atmosenv.2020.117403, 2020.

824   Thalman, R., de Sa, S. S., Palm, B. B., Barbosa, H. M. J., Poehlker, M. L., Alexander, M. L., Brito, J.,

825   Carbone, S., Castillo, P., Day, D. A., Kuang, C., Manzi, A., Ng, N. L., Sedlacek, A. J., Souza, R.,

826   Springston, S., Watson, T., Poehlker, C., Poeschl, U., Andreae, M. O., Artaxo, P., Jimenez, J. L.,

827   Martin, S. T., and Wang, J.: CCN activity and organic hygroscopicity of aerosols downwind of an

828   urban region in central Amazonia: seasonal and diel variations and impact of anthropogenic emissions,

829   17, 11779–11801, https://doi.org/10.5194/acp-17-11779-2017, 2017.

830 Wang, Y., Chen, J., Wang, Q., Qin, Q., Ye, J., Han, Y., Li, L., Zhen, W., Zhi, Q., Zhang, Y., and Cao,
831 J.: Increased secondary aerosol contribution and possible processing on polluted winter days in China,
832 Environment International, 127, 78–84, https://doi.org/10.1016/j.envint.2019.03.021, 2019.

833 Wang, Z., Cheng, Y., Ma, N., Mikhailov, E., Pöschl, U., and Su, H.: Dependence of the hygroscopicity
834 parameter κ on particle size, humidity and solute concentration: implications for laboratory
835 experiments, field measurements and model studies, Atmos. Chem. Phys. Discuss., 2017, 1–33,
836 https://doi.org/10.5194/acp-2017-253, 2017.

837 Wiedensohler, A., Cheng, Y. F., Nowak, A., Wehner, B., Achtert, P., Berghof, M., Birmili, W., Wu,
838 Z. J., Hu, M., Zhu, T., Takegawa, N., Kita, K., Kondo, Y., Lou, S. R., Hofzumahaus, A., Holland, F.,
839 Wahner, A., Gunthe, S. S., Rose, D., Su, H., and Poeschl, U.: Rapid aerosol particle growth and
840 increase of cloud condensation nucleus activity by secondary aerosol formation and condensation: A
841 case study for regional air pollution in northeastern China, 114, D00G08,
842 https://doi.org/10.1029/2008JD010884, 2009.

843 Williams, B. J., Goldstein, A. H., Kreisberg, N. M., Hering, S. V., Worsnop, D. R., Ulbrich, I. M.,
844 Docherty, K. S., and Jimenez, J. L.: Major components of atmospheric organic aerosol in southern
845 California as determined by hourly measurements of source marker compounds, Atmos. Chem. Phys.,
846 10, 11577–11603, https://doi.org/10.5194/acp-10-11577-2010, 2010.

847 Wu, Z. J., Poulain, L., Birmili, W., Groess, J., Niedermeier, N., Wang, Z. B., Herrmann, H., and
848 Wiedensohler, A.: Some insights into the condensing vapors driving new particle growth to CCN sizes
849 on the basis of hygroscopicity measurements, 15, 13071–13083, https://doi.org/10.5194/acp-15-
850 13071-2015, 2015.

851 Wu, Z. J., Zheng, J., Shang, D. J., Du, Z. F., Wu, Y. S., Zeng, L. M., Wiedensohler, A., and Hu, M.:
852 Particle hygroscopicity and its link to chemical composition in the urban atmosphere of Beijing, China,
853 during summertime, Atmos. Chem. Phys., 16, 1123–1138, https://doi.org/10.5194/acp-16-1123-2016,
854 2016.

855 Xu, W., Han, T., Du, W., Wang, Q., Chen, C., Zhao, J., Zhang, Y., Li, J., Fu, P., Wang, Z., Worsnop,
856 D. R., and Sun, Y.: Effects of Aqueous-Phase and Photochemical Processing on Secondary Organic
857 Aerosol Formation and Evolution in Beijing, China, Environ. Sci. Technol., 51, 762–770,
858 https://doi.org/10.1021/acs.est.6b04498, 2017a.

859 Xu, W., Croteau, P., Williams, L., Canagaratna, M., Onasch, T., Cross, E., Zhang, X., Robinson, W.,
860 Worsnop, D., and Jayne, J.: Laboratory characterization of an aerosol chemical speciation monitor

with PM2.5 measurement capability, Aerosol Science and Technology, 51, 69–83, https://doi.org/10.1080/02786826.2016.1241859, 2017b.

Xu, W., Sun, Y., Wang, Q., Zhao, J., Wang, J., Ge, X., Xie, C., Zhou, W., Du, W., Li, J., Fu, P., Wang, Z., Worsnop, D. R., and Coe, H.: Changes in Aerosol Chemistry From 2014 to 2016 in Winter in Beijing: Insights From High-Resolution Aerosol Mass Spectrometry, Journal of Geophysical Research: Atmospheres, 124, 1132–1147, https://doi.org/10.1029/2018JD029245, 2019.

Xu, W. Q., Sun, Y. L., Chen, C., Du, W., Han, T. T., Wang, Q. Q., Fu, P. Q., Wang, Z. F., Zhao, X. J., Zhou, L. B., Ji, D. S., Wang, P. C., and Worsnop, D. R.: Aerosol composition, oxidation properties, and sources in Beijing: results from the 2014 Asia-Pacific Economic Cooperation summit study, Atmos. Chem. Phys., 15, 13681–13698, https://doi.org/10.5194/acp-15-13681-2015, 2015.

Yu, F., Luo, G., Nair, A. A., Schwab, J. J., Sherman, J. P., and Zhang, Y.: Wintertime new particle formation and its contribution to cloud condensation nuclei in the Northeastern United States, Atmos. Chem. Phys., 20, 2591–2601, https://doi.org/10.5194/acp-20-2591-2020, 2020.

Yue, D., Zhong, L., Zhang, T., Shen, J., Yuan, L., Ye, S., Zhou, Y., and Zeng, L.: Particle Growth and Variation of Cloud Condensation Nucleus Activity on Polluted Days with New Particle Formation: A Case Study for Regional Air Pollution in the PRD Region, China, 16, 323–335, https://doi.org/10.4209/aaqr.2015.06.0381, 2016.

Zhang, F., Li, Y., Li, Z., Sun, L., Li, R., Zhao, C., Wang, P., Sun, Y., Liu, X., Li, J., Li, P., Ren, G., and Fan, T.: Aerosol hygroscopicity and cloud condensation nuclei activity during the AC3Exp campaign: implications for cloud condensation nuclei parameterization, Atmos. Chem. Phys., 14, 13423–13437, https://doi.org/10.5194/acp-14-13423-2014, 2014.

Zhang, F., Li, Z., Li, Y., Sun, Y., Wang, Z., Li, P., Sun, L., Wang, P., Cribb, M., Zhao, C., Fan, T., Yang, X., and Wang, Q.: Impacts of organic aerosols and its oxidation level on CCN activity from measurement at a suburban site in China, 16, 5413–5425, https://doi.org/10.5194/acp-16-5413-2016, 2016.

Zhang, F., Ren, J., Fan, T., Chen, L., Xu, W., Sun, Y., Zhang, R., Liu, J., Jiang, S., Jin, X., Wu, H., Li, S., Cribb, M. C., and Li, Z.: Significantly enhanced aerosol CCN activity and number concentrations by nucleation-initiated haze events: a case study in urban Beijing, Journal of Geophysical Research: Atmospheres, n/a, https://doi.org/10.1029/2019JD031457, 2019.

Zhang, Q., Jimenez, J. L., Canagaratna, M. R., Ulbrich, I. M., Ng, N. L., Worsnop, D. R., and Sun, Y.: Understanding atmospheric organic aerosols via factor analysis of aerosol mass spectrometry: a review,

892 Analytical and Bioanalytical Chemistry, 401, 3045–3067, https://doi.org/10.1007/s00216-011-5355-
893 y, 2011.

894 Zhang, R., Khalizov, A., Wang, L., Hu, M., and Xu, W.: Nucleation and Growth of Nanoparticles in
895 the Atmosphere, 112, 1957–2011, https://doi.org/10.1021/cr2001756, 2012.

896 Zhao, G., Tan, T., Zhao, W., Guo, S., Tian, P., and Zhao, C.: A new parameterization scheme for the
897 real part of the ambient urban aerosol refractive index, 19, 12875–12885, https://doi.org/10.5194/acp-
898 19-12875-2019, 2019.

899

Figures:

901
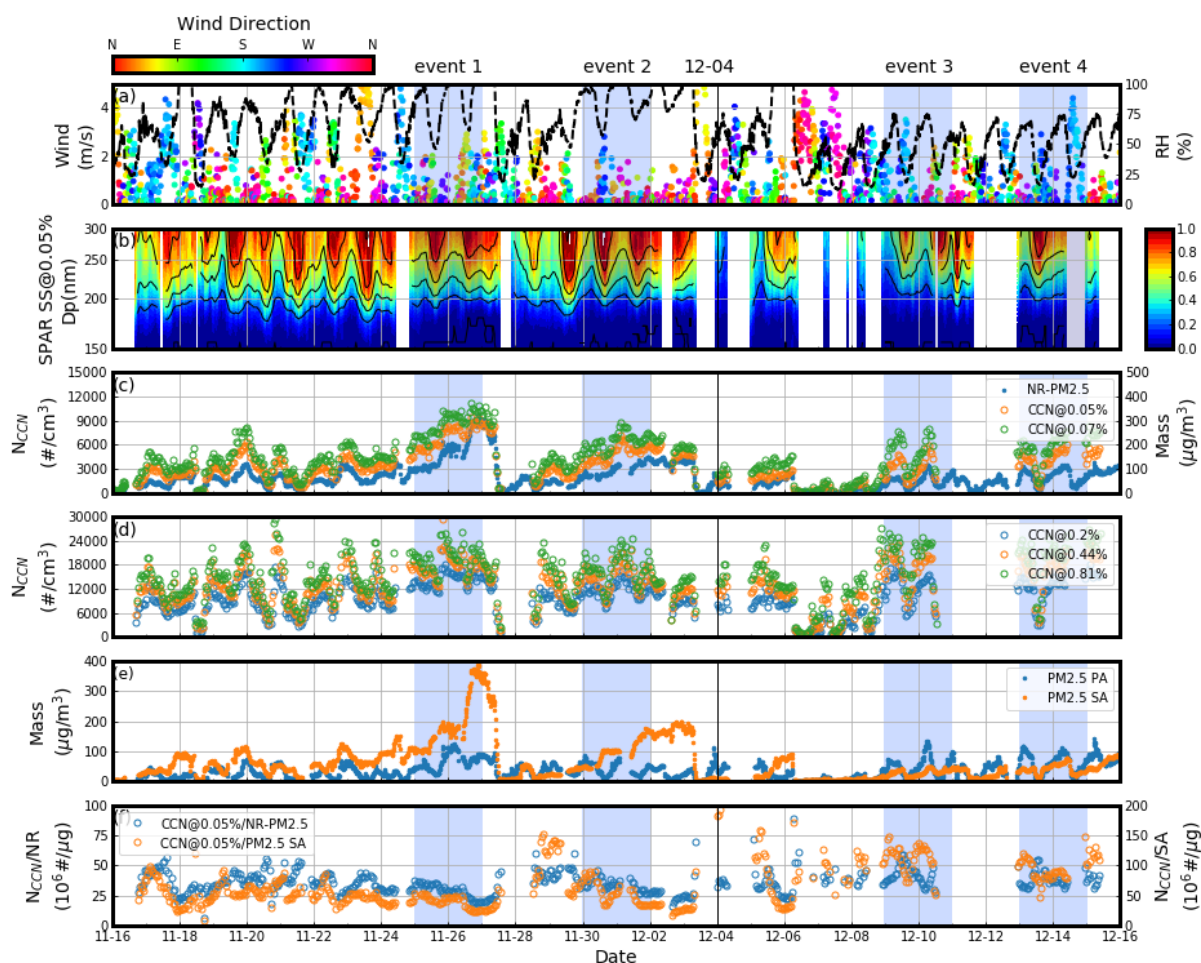
Fig 1. Overview of the measurements during the campaign: (a) dots represent wind speed with color indicating wind direction, and black lines represent RH; (b) SPAR under SS of 0.05%; (c) blue, green and yellow dots represent N_{CCN} under SS of 0.05% and 0.07%, and mass concentration of NR-PM2.5, respectively; (d) blue, green and yellow dots represent N_{CCN} under SS of 0.2%, 0.44% and 0.81%, respectively; (e) blue and yellow dots represent mass concentration of $PM_{2.5}$ PA and $PM_{2.5}$ SA respectively; (f) blue and yellow dots represent ratio between N_{CCN} and mass concentration of NR-$PM_{2.5}$ and $PM_{2.5}$ SA, respectively. There were four events with significant enhancements of N_{CCN} during the blue shaded periods.

910

911
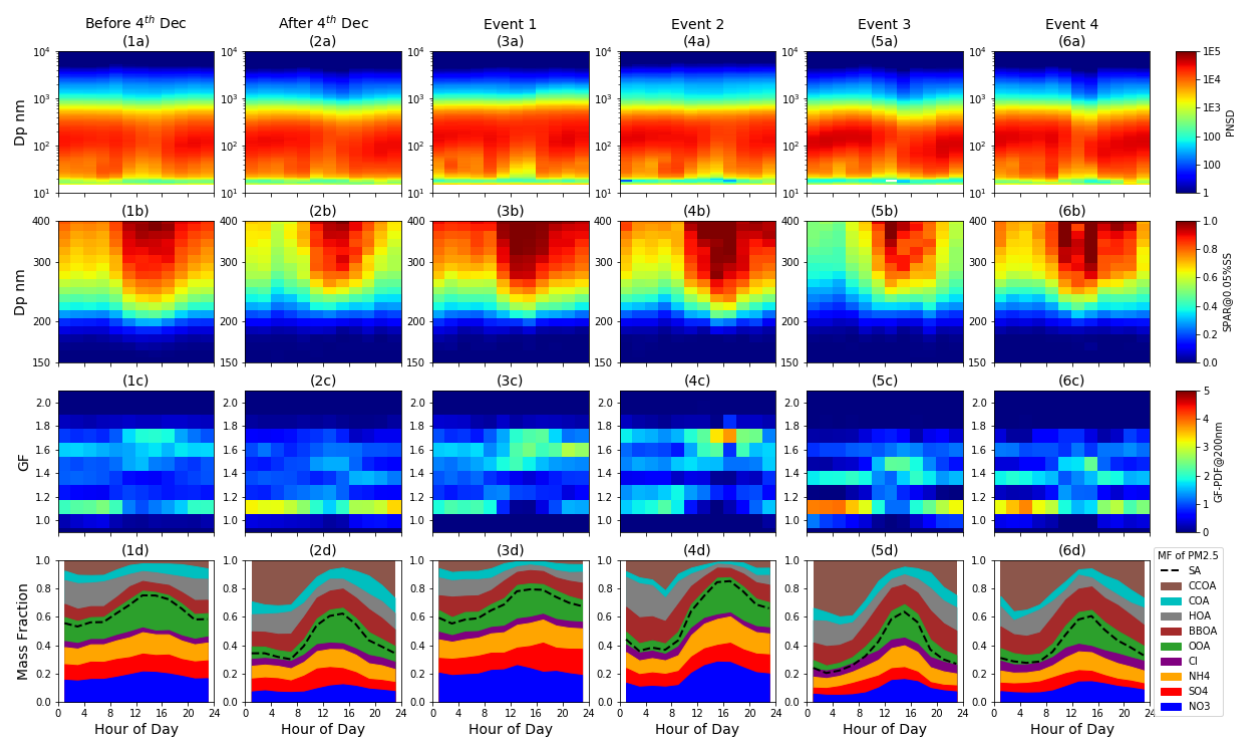
Fig 2. Diurnal variation of (a) PNSD, (b) SPAR at SS of 0.05%, (c) GF-PDF at 200 nm and (d) mass

fraction of different PM$_{2.5}$ chemical species during high RH periods before 4th Dec (1), low RH

periods after 4th Dec (2) and the four events (3-6), including OA factors: hydrocarbon-like OA

(HOA), cooking OA (COA), biomass burning OA (BBOA), coal combustion OA (CCOA), and

oxygenated OA (OOA).

917

918
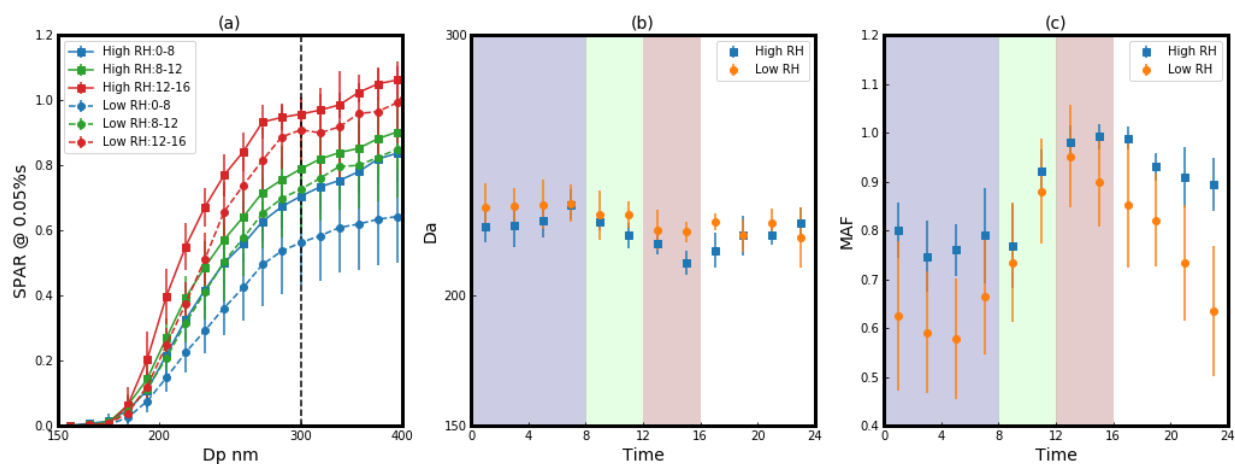
919 Fig 3. (a) The averages of SPAR curves at SS of 0.05% in three different time periods (blue: 0:00-
920 8:00; green: 8:00-12:00; red: 12:00-16:00) during high (squares with solid line, event 1 and 2) and low
921 (dots with dashed line, event 3 and 4) RH events. Diurnal variation of (b) D_a and (c) MAF under high
922 (blue) and low (yellow) RH conditions. The blue, green and red shades correspond to with the three
923 periods in (a & d). Error bars indicate the standard deviations of data.

924
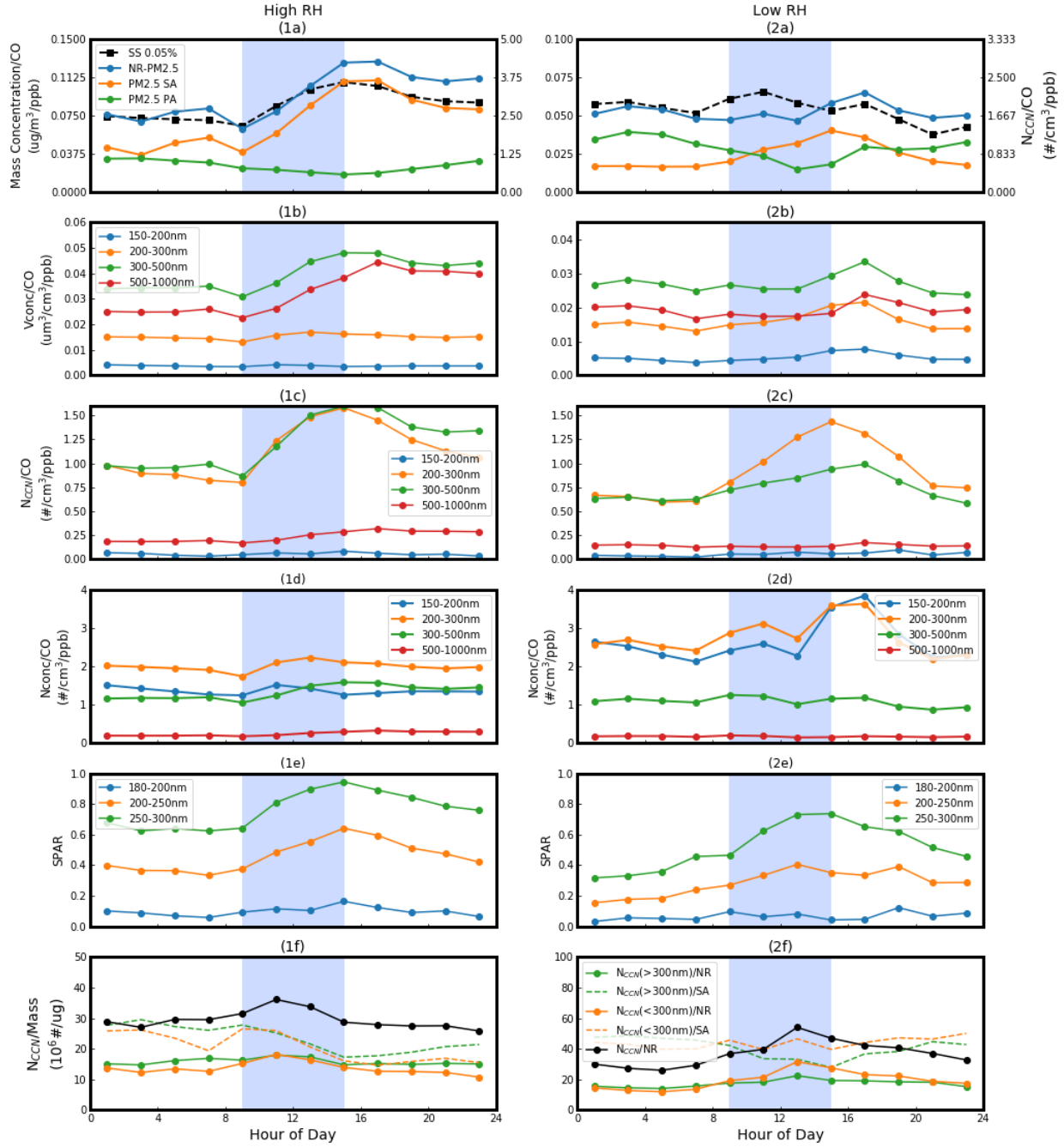
Fig 4. During different RH events, the average diurnal variation of (a) the ratios between particle

mass concentration (dots with solid lines; blue: NR-PM$_{2.5}$; yellow: PM$_{2.5}$ SA; green: PM$_{2.5}$ PA) and

CO concentration, and the ratio between N$_{CCN}$ at SS of 0.05% and CO concentration (squares with

solid line); (b) the ratios between particle volume concentration (Vconc) of different particle size

range (indicated by colors) and CO concentration; (c) the ratios between N$_{CCN}$ of different particle

size range at SS of 0.05% (indicated by colors) and CO concentration; (d) the ratios between particle

number concentration (Nconc) of different particle size range (indicated by colors) and CO

concentration; (e) SPAR of different particle size range (indicated by colors); (f) the ratios between

N$_{CCN}$ at SS of 0.05% (black: bulk N$_{CCN}$; yellow: N$_{CCN}$ with particle size larger than 300 nm; blue:

934   N_{CCN} with particle size smaller than 300 nm) and mass concentration of NR-PM$_{2.5}$ SA and the ratios

935   between N_{CCN} and mass concentration of NR-PM$_{2.5}$ (dashed lines).

936
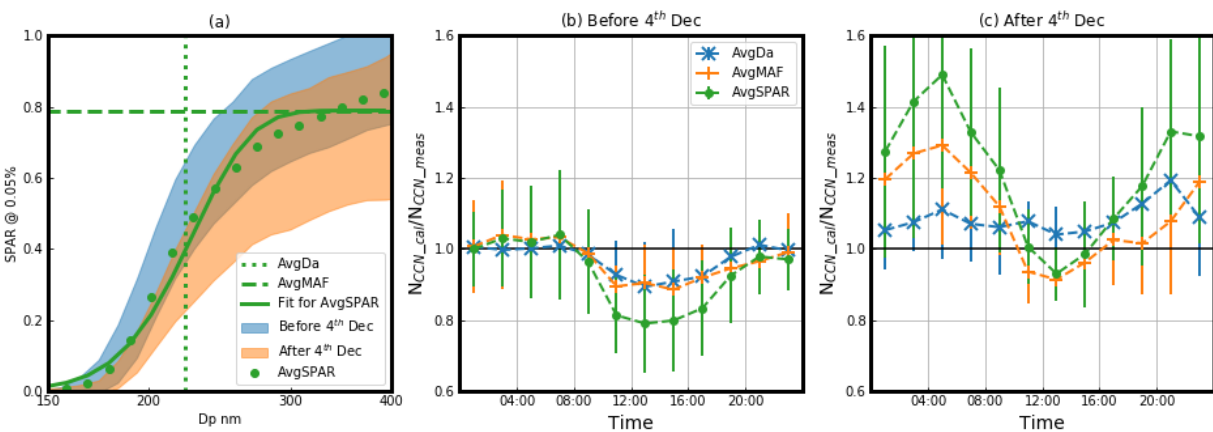
937

938 Fig 5. (a) The averaged SPAR at SS of 0.05% during the campaign (green scatters), the

939 corresponding fitting curve (green line) and the averaged fitting parameters (dotted line for D_a and

940 dashed line for MAF). The blue and yellow shaded areas represent the variations of SPAR before 4th

941 Dec and after 4th Dec, respectively. The ratio between calculated N_{CCN} and measured N_{CCN} under (b)

942 before and (c) after 4th Dec. Bars represent one standard deviation and colors represent different

943 calculation of SPAR curves: green represent average SPAR during the campaign (AvgSPAR),

944 yellow represent SPAR calculated with average D_a and real-time MAF (AvgDa) and blue represent

945 SPAR calculated with average MAF and real-time D_a (AvgMAF).

946
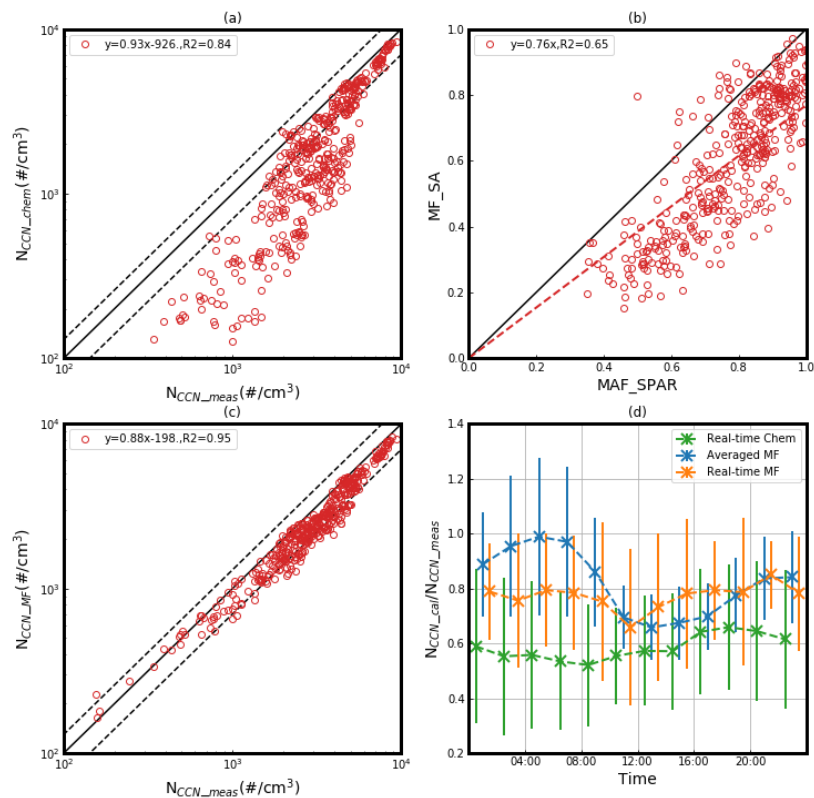
Fig 6. (a) The comparison between calculated N_{CCN} based on κ derived from bulk particle chemical compositions (N_{CCN_chem}) and measured N_{CCN} at SS of 0.05%. (b) The correlation between MAF and mass fraction of secondary aerosol (MF_{SA}). (c) the comparison between calculated N_{CCN} based on SPAR derived from real-time MF_{SA} and average D_a (N_{CCN_MF}) and measured N_{CCN}. The black dashed lines represent the relative deviation of 30%. (d) the diurnal variations of the ratio between the calculated and measured N_{CCN} during the whole campaign based on different methods (green: N_{CCN_chem}; blue: N_{CCN} calculated based on SPAR derived from averaged MF_{SA} and average D_a; yellow: N_{CCN_MF}).

955

956
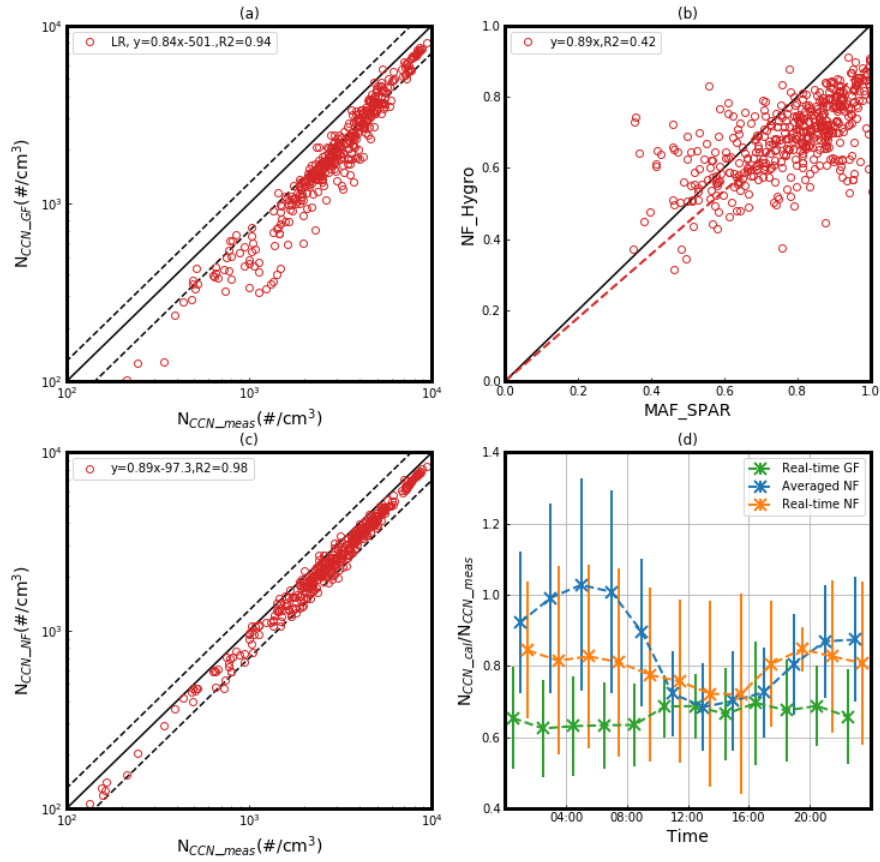
Fig 7. (a) The comparison between calculated N_{CCN} based on κ derived from bulk GF at 200 nm (N_{CCN_GF}) and measured N_{CCN} at SS of 0.05%. (b) The correlation between MAF and number fraction of hygroscopic particles (NF_{hygro}, GF>1.2). (c) The comparison between calculated N_{CCN} based on SPAR derived from real-time NF_{hygro} and average D_a (N_{CCN_NF}) and measured N_{CCN}. The black dashed lines represent the relative deviation of 30%. (d) the diurnal variations of the ratio between the calculated and measured N_{CCN} during the whole campaign based on different methods (green: N_{CCN_GF}; blue: N_{CCN} based on SPAR derived from averaged NF_{hygro} and average D_a; yellow: N_{CCN_NF}).